Global and Planetary Change 256 (2026) 105176

Contents lists available at ScienceDirect

Global and Planetary Change

journal homepage: www.elsevier.com/locate/gloplacha

The Holocene evolution of a sinkhole on the Southeast Red Sea Shelf: From saline palaeolake to stratified marine setting

Francesca Paraschos [a,b,c,*], Melissa A. Berke [d], Andreas Koutsodendris [c], Oliver Friedrich [c], Spyros Sergiou [b], Maria Geraga [b], Helen Kaberi [a], Ross Williams [d], Geoffrey Bailey [e,f], Jörg Pross [c], Dimitris Sakellariou [a]

[a] Institute of Oceanography, Hellenic Center for Marine Research, 46.7km Athens-Sounio Ave, 19013 Athens, Greece
[b] Laboratory of Marine Geology and Physical Oceanography, Department of Geology, University of Patras, 26504 Patras, Greece
[c] Institute of Earth Sciences, Heidelberg University, Im Neuenheimer Feld 234, 69120 Heidelberg, Germany
[d] Department of Civil and Environmental Engineering and Earth Sciences, University of Notre Dame, 156 Fitzpatrick Hall, Notre Dame, IN 46556, USA
[e] Department of Archaeology, King's Manor, University of York, York YO1 7EP, United Kingdom
[f] College of Humanities, Arts and Social Sciences, Flinders University, Adelaide, Australia

ARTICLE INFO

Editor: Dr. Fabienne Marret-Davies

Keywords:
Carbonate platforms
Sea-level change
Palaeoclimate
Submerged landscapes
Marine geoarchaeology
Sinkholes
GDGTs
XRF-CS
Foraminifera

ABSTRACT

The submerged coastal landscapes of the southern Red Sea preserve key archives of postglacial environmental change, shaped by sea-level rise and shifting hydroclimatic regimes. On the southeast shelf, the Farasan Deep—a deep, morphologically isolated sinkhole—records a rare transition from a saline palaeolake to a stratified marine setting. We present a new multiproxy record from sediment core FA24, integrating lipid biomarkers (branched and isoprenoid glycerol dialkyl glycerol tetraethers [GDGTs]), XRF-core scanning, LOI, sedimentology, and micropalaeontology to reconstruct water-column structure, redox dynamics, and microbial and faunal shifts over the past 11.8 kyr. Results reveal three distinct phases. Phase I (11.8–8.7 ka) reflects hydrographic isolation, strong stratification, and sustained bottom-water anoxia. Laminated organic-rich sediments, diatom mats, low foraminiferal counts, and biomarker evidence indicate persistent oxygen depletion and a distinct microbial ecology. Phase II (8.7–6.7 ka) captures transitional dynamics, marked by episodic marine incursions, fluctuating redox conditions, rising GDGT inputs, and sporadic foraminiferal reappearances. Phase III (post-6.7 ka) signals full marine reconnection with stable stratification, persistent bottom-water anoxia, increased microbial lipid production, and benthic foraminiferal assemblages dominated by infaunal taxa. The Farasan Deep record sheds light on the timing and feedbacks of postglacial marine reconnection in marginal basins. Beyond its regional context, it provides a globally relevant analogue for redox-sensitive carbon cycling, stratification feedbacks, and GDGT proxy behavior in semi-enclosed systems. These findings further underscore the geoarchaeological significance of submerged landscapes and support improved palaeoclimate reconstructions in hydroclimatically sensitive marine settings.

1. Introduction

Submerged coastal landscapes have increasingly been recognized as valuable archives for advancing our understanding of climatic variability, sea-level dynamics, and past human development (Bailey et al., 2020; Faure et al., 2002; Flemming Nicholas et al., 2017; Hale et al., 2021). From a geoarchaeological perspective, they may hold important evidence of early human activity, as global sea level remained below present level for 95 % of the last glacial-interglacial cycle (Grant et al., 2014), and thus, for much of human history (Bailey and Cawthra, 2023). The Red Sea basin stands out as a particularly salient example, having emerged as a key region for the investigation of Quaternary sea-level fluctuations and patterns of early human dispersal and settlement (Bailey et al., 2015; Lambeck et al., 2011; Rohling et al., 2013). In

* Corresponding author at: Institute of Oceanography, Hellenic Centre for Marine Research, 46.7km Athens-Sounio Ave, 19013 Athens, Greece.
E-mail addresses: fparaskos@hcmr.gr, francesca.paraschos@geow.uni-heidelberg.de (F. Paraschos).

https://doi.org/10.1016/j.gloplacha.2025.105176
Received 29 July 2025; Received in revised form 3 November 2025; Accepted 9 November 2025
Available online 10 November 2025

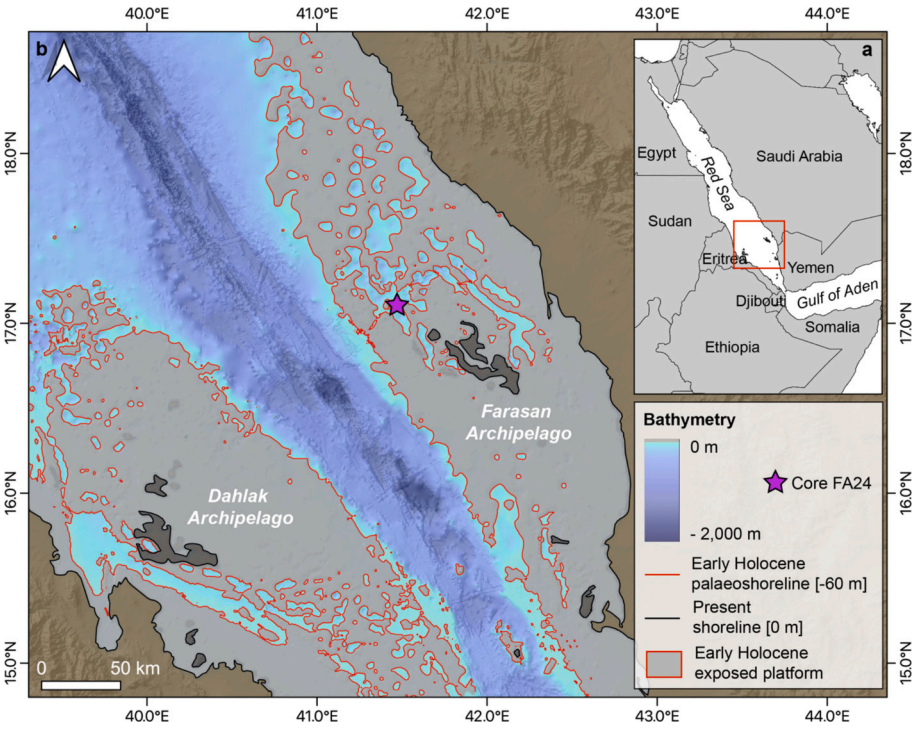

Fig. 1. Map of the study area. a) Overview on the wider study area in the southern Red Sea, and b) bathymetry of the area surrounding the Farasan Archipelago. The early Holocene (ca. 11.7 ka) palaeoshoreline, at -60 meters below present, is depicted in red, while the respective exposed continental shelf is shown in gray. The purple star marks the location of Core FA24 within the Farasan Deep, located within the inner part of the shelf, approximately 90 km off the Saudi Arabian coast. The bathymetric map was constructed through a combination of data from the DISPERSE cruise (Sakellariou et al., 2019) and the GEBCO Gridded Bathymetry (GEBCO 2024 Grid). The early Holocene palaeoshoreline was reconstructed from the Red Sea Relative Sea Level data of Grant et al. (2012) for 12–7 kyr, and Al-Mikhlafi et al. (2021), Arz et al. (2007) for 7–0 kyr.

addition to its geoarchaeological significance, the Red Sea offers a unique opportunity to investigate how tropical coastal regions have responded to past environmental forcing, notably extreme hydrographic and hydrologic variability (Rohling et al., 2013).

Within this broader context, the Farasan Bank on the southeastern shelf of the Red Sea represents a compelling subregion due to its distinct geomorphological configuration and proximity to the basin's connection to the Indian Ocean via the Bab al Mandab strait. The complex topography of the Farasan carbonate platform (Fig. 1) hosts a multitude of circular and elongate bathymetric depressions (Bailey et al., 2015; Sakellariou et al., 2019). These depressions represent collapse structures formed by the dissolution of near-surface evaporitic domes and are widespread across both the Farasan Archipelago on the Saudi Arabian shelf as well as on the Dahlak Archipelago on the Eritrean shelf (Bailey et al., 2015; Bantan, 1999; Sakellariou et al., 2019). While the precise timing of their formation remains uncertain, geophysical evidence indicates that many of these depressions existed prior to late Pleistocene sea-level lowstands and remained water-filled, potentially offering favourable conditions for early human dispersal and settlement (Bailey, 2015; Bailey et al., 2019; Bailey, 2015; Sakellariou et al., 2019). Marine sedimentation along the shelf is predominantly confined within these depressions, which act as natural sediment traps and preserve high-resolution palaeoenvironmental and palaeoclimatic information during sea-level lowstands (Sakellariou et al., 2019). In these enclosed depressions, prolonged environmental isolation and hydrographic stratification likely promoted the development of a unique ecological niche and distinct microbial communities (Klein et al., 2025).

Our primary aim in this paper is to reconstruct the palaeoenvironmental evolution of the Farasan Deep, one of several bathymetric depressions along the southern Red Sea carbonate shelf that transformed into isolated palaeolakes during the low sea-level periods of the late Pleistocene (Fig. 1). Despite the plethora of studies reconstructing past oceanographic and hydroclimatic conditions within the Red Sea basin (Arz et al., 2003; Bouilloux et al., 2013; Edelman-Furstenberg et al., 2001; Legge et al., 2006), no palaeoenvironmental reconstructions exist for these coastal palaeolake settings. We base our investigation on a novel multiproxy reconstruction of marine sediment Core FA24 recovered from a depth of 500 m within the Farasan Deep and place particular emphasis on membrane lipid biomarkers such as the glycerol dialkyl glycerol tetraethers (GDGTs). These biomarkers have emerged as powerful tools for the reconstruction of microbial communities and depositional conditions (Damsté et al., 2000; De Jonge et al., 2016; Schouten et al., 2013; Weijers et al., 2006a, 2006b), but research on their distributions in Red Sea sediments has been largely restricted to surface samples and deep-water settings beyond the continental shelf (Biton et al., 2010; Trommer et al., 2011; Trommer et al., 2010; Trommer et al., 2009; Varma et al., 2024b). We complement GDGT analysis with independent palaeoenvironmental proxies, including x-ray fluorescence core scanning (XRF-CS) derived elemental ratios, loss-on-ignition (LOI), and semi-quantitative microfaunal analysis, In this way, we aim to disentangle and understand local depositional processes and ecological dynamics and reconstruct the palaeoenvironmental evolution of this basin, thereby contributing valuable environmental context to ongoing discussions regarding the potential geoarchaeological significance of these palaeolake structures.

Core FA24 thus provides the first-ever record from the numerous late Pleistocene palaeolake basins on the southeastern Red Sea shelf. In the absence of other sedimentary archives from comparable environments, it offers a unique baseline for understanding environmental change in these depositional settings. Moreover, findings from such marginal marine systems may offer analogues for the comprehension of palaeoenvironmental dynamics in other tropical coastal regions globally.

2. Lipid biomarkers

Archaeal and bacterial communities, the primary producers of many preserved membrane-spanning lipids, offer key insights into ecological structure and environmental conditions such as oxygenation, salinity, and nutrient availability in both modern and ancient environments (Damsté et al., 2000; De Jonge et al., 2016; Schouten et al., 2013; Weijers et al., 2006a, 2006b). Understanding shifts in these communities is essential not only for reconstructing redox dynamics and stratification regimes, but also for tracking broader changes in hydroclimatic forcing and marine-terrestrial interactions. **Isoprenoid GDGTs** (isoGDGT-0 to -4, crenarchaeol, and its isomer), originally described in Archaea (De Rosa and Gambacorta, 1988; Koga et al., 1993), are now known to be primarily produced by ammonia-oxidizing archaea (AOA) of the phylum *Nitrososphaerota* (formerly *Thaumarchaeota*) in the Genome Taxonomy Database. These organisms are ubiquitous in modern oceans (Pitcher et al., 2011; Schouten et al., 2013; Sinninghe Damsté et al., 2002) and may constitute up to 20–40% of marine picoplankton biomass (Fuhrman et al., 1992; Karner et al., 2001; Schattenhofer et al., 2009). Closely related compounds, **hydroxylated isoprenoid GDGTs (OH-isoGDGTs)**, are also believed to be produced predominantly by *Thaumarchaeota* (Liu et al., 2012; Sinninghe Damsté et al., 2012b). These lipids are generally more abundant in high-latitude settings and are hypothesized to enhance membrane stability under low-temperature conditions (Huguet et al., 2013; Huguet et al., 2006).

In contrast, **branched GDGTs (brGDGTs)** were long considered exclusive biomarkers of anaerobic soil bacteria, reaching marine sediments solely through terrestrial runoff (Damsté et al., 2000; Hopmans et al., 2004; Weijers et al., 2006a, 2006b). However, a growing body of evidence now supports their **potential for in situ sedimentary production** under specific marine conditions (De Jonge et al., 2016; Peterse et al., 2009; Sinninghe Damsté, 2016; Weijers et al., 2014; Xiao et al., 2016), particularly in shallow shelf settings with elevated productivity and rapid sedimentation. Variability in microbial communities shaped by environmental isolation and extreme environmental conditions can modulate GDGT assemblages in ways that challenge open-ocean signals, as already evidenced by studies in the Red Sea (Biton et al., 2010; Ionescu et al., 2009; Klein et al., 2025; Qian et al., 2011; Trommer et al., 2009).

3. Study area

The Red Sea is a semi-enclosed and elongated basin within the arid Saharan-Arabian desert belt, connected to the Indian Ocean via the narrow and shallow Bab-al-Mandab strait (~25 km wide, ~310 m deep) (Morcos, 1970) (Fig. 1). Water-mass exchange with the Gulf of Aden is primarily regulated by the 137 m-deep Hanish Sill, which is located just north of the strait and forms the shallowest constriction in the channel (Werner and Lange, 1975). Combined with eustatic controls, high net evaporation (2000 mm yr^{-1}), low precipitation (10–200 mm yr^{-1}), and negligible seasonal runoff contribute to the formation of warm, highly saline water masses within the basin (Sofianos and Johns, 2007). Seasonal variability of the South Asian monsoon system drives the reversal of surface and intermediate circulation in the southern Red Sea (e.g., Yao et al., 2014, 2014a). In summer (June–September), southwesterly winds induce upwelling in the Gulf of Aden, enabling the northward intrusion of cool, nutrient-rich Gulf of Aden Intermediate Water (GAIW). This influx of GAIW promotes the development of mesotrophic conditions in the southern Red Sea (Churchill et al., 2015; Raitsos et al., 2013; Sofianos and Johns, 2007). Despite the bathymetric barrier of the Hanish Sill, oceanographic evidence suggests that a continuous connection with the Gulf of Aden has persisted for the past 500 kyr (Grant et al., 2014; Lambeck et al., 2011; Siddall et al., 2003). During glacial sea-level lowstands, however, this connectivity was strongly reduced, resulting in marked alterations in water circulation and ecological dynamics (Sergiou et al., 2022a, 2022b; Trommer et al., 2011).

Swath bathymetry of the area reveals that Core FA24 (17° 05.680' N, 41° 28.125' E; 500 m water depth) was recovered from a ~ 500 m deep, irregularly shaped sinkhole, the Farasan Deep, and is surrounded by a flat shelf at 70–90 m depth (Figs 1 and 2a). The Farasan Deep is interpreted as a collapse structure formed by the dissolution of underlying Miocene (Sakellariou et al., 2019). The composite seismic profile displays a complex seismic stratigraphy, with the sedimentary infill consisting of two sedimentary units separated by a significant unconformity (Fig. 2b). The lower Unit 2 has a minimum thickness of 200 milliseconds, or approximately 150 m, and dips northwards, towards the northern and almost vertical margin of the sinkhole. The deposits of the overlying Unit 1 are nearly horizontal and unconformably cover the

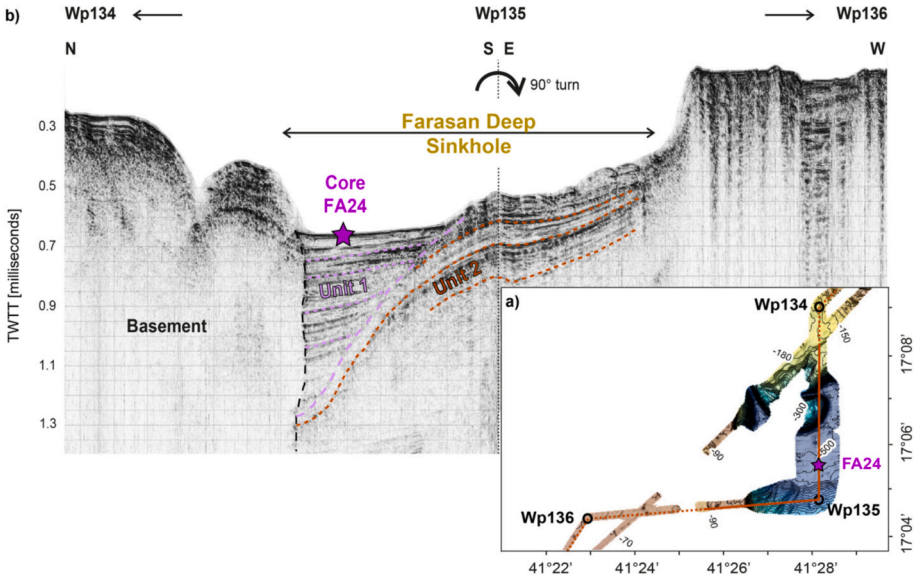

Fig. 2. Core location and seismic context of the Farasan Deep sinkhole. **(a)** Location of Core FA24 on a swath bathymetry map acquired in 2021 aboard R/V *'AEGAEO'*. The core was collected from a depth of 500 m within an enclosed depression, surrounded by a flat, shallow carbonate shelf. The brown line indicates the seismic profile transect shown in (b). **(b)** Airgun seismic profile across the 500 m-deep sinkhole. Wp = Waypoint.

northward-dipping layers of Unit 2 while filling the space between the latter and the northern margin. The maximum thickness of Unit 1 exceeds 600 milliseconds or, roughly, 450 m.

4. Material and methods

4.1. Core FA24 and chronology

Gravity Core FA24 (17° 05.680' N, 41° 28.125' E, 500 m water depth) was retrieved in 2021 with the R/V 'AEGAEO' as part of a follow-up to the DISPERSE project which conducted coring in the region in 2013 (Bailey, 2015; Bailey et al., 2015). A total of 4.03 m of sediment was recovered, while a visual core description based on sediment colour and texture identified four main lithological units (A–D), ranging from laminated, flocculent sediments in the lower core to more compact, homogeneous silts of marine origin in the uppermost section (Fig. 3). These units are interspersed with distinct light-colored layers that vary in composition and texture (L1–L15) (Fig. 3). For a detailed description of the lithological units and interbedded layers, see Text S1 and Fig. S1.

For the construction of the chronological framework ten samples were taken for ^{14}C AMS dating. Specifically, seven samples of ca. 1–6 mg of planktic foraminifera tests (consisting of the species *G. ruber*, *T. sacculifer and G. siphonifera)* and three samples of ca. 0.3–0.8 mg of bivalves were analysed at the LARA laboratory of the University of Bern (Table 1). Three bivalve samples were selected to constrain the age of a core section (within Units A and B; Fig. S1) lacking both planktic and benthic foraminifera tests. The anomalously old ages of the bivalve may reflect localized reservoir effects from the uptake of older carbon during periods of lake isolation. Alternatively, juvenile bivalves could have been introduced from nearby littoral zones during fluvial episodes. However, the absence of reworking or high-energy deposition in Phase I sediments suggests that these ages are more likely due to geochemical or ecological 14C complexities than physical disturbance. Given these uncertainties, the bivalve-derived ages were excluded from the core's chronostratigraphy. The calibration of all ^{14}C ages and the Bayesian age model development were performed with the MARINE20 calibration curve (Heaton et al., 2020) within the CRAN R package rbacon (v.3.0.0)

Table 1
AMS ^{14}C ages, calibrated age ranges (2σ), and calibrated median ages obtained on planktic foraminifera tests and bivalves. The calibrated ages are calculated through the Calib 8.2 Software and the MARINE20 Calibration curve with a ΔR= -59 ± 38. The samples marked with an asterisk were eventually discarded from the age-model due to age reversals.

Lab Code	Core depth (cm)	^{14}C Age (yr BP)	Calibrated Age Range (2σ) (cal yr BP)	Calibrated Median Age Probability (cal yr BP)	Remarks
BE-19456.1.1	5.5	1394 ± 31	675–982	834	Planktic foraminifera
BE-19457.1.1	40.5	2171 ± 31	1477–1831	1652	Planktic foraminifera
BE-17734.1.1	77.5	6139 ± 71	6222–6658	6435	Planktic foraminifera
BE-17735.1.1	139.5	8544 ± 51	8816–9286	9059	Planktic foraminifera
BE-17736.1.1	216.5	8170 ± 50	8349–8777	8543	Planktic foraminifera
BE-19458.1.1	224.5	10173 ± 144	10724-11678	11197	Bivalves*
BE-19459.1.1	289.5	9022 ± 198	9130-10181	9650	Bivalves*
BE-19460.1.1	303.5	8930 ± 159	9081-10007	9521	Bivalves*
BE-17737.1.1	325.5	8479 ± 106	8603–9286	8960	Planktic foraminifera
BE-19461.1.1	375.5	10349 ± 158	10992–11986	11454	Planktic foraminifera

(Blaauw and Christen, 2011a, 2011b). The nearest available local reservoir effect of ΔR= -59 ± 38 (Southon et al., 2002) was applied. The outlying ^{14}C AMS age of 8544 ± 51 yrs, obtained at 139.5 cm, was not excluded from the Bayesian age model which utilises a Student-*t* model to calibrate ^{14}C AMS ages. The heavier tails of the Student-*t* distribution can accommodate wider data variations and enhance the robustness of age estimations against the presence of potential outliers (Blaauw and Christen, 2011). Sea-level fluctuations have been previously reported to

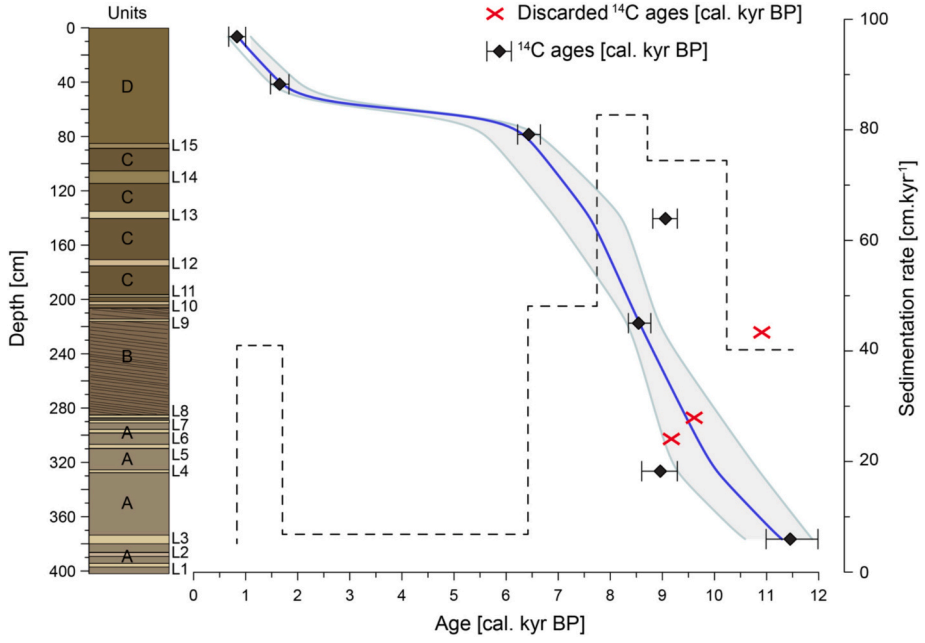

Fig. 3. Bayesian age model and lithological units of Core FA24. Black diamonds and error bars illustrate the calibrated ^{14}C AMS-ages and respective errors. The calibrated ages of the discarded bivalve samples are shown in red. The thick blue line depicts the median age-depth model, while gray lines show the 95 % confidence intervals calculated through the Bacon approach. The dashed black line indicates the linear sedimentation rates calculated between the calibrated ^{14}C AMS ages. Lithological units (A–D) and layers (L1–L15) of Core FA24 plotted against core depth.

affect residence times and thus reservoir ages within the Red Sea, further highlighting the complexities of radiocarbon dating within the region (Biton et al., 2008; Bouilloux et al., 2013; Rohling et al., 2008; Siddall et al., 2004; Trommer et al., 2010). Bearing this in mind, we recognise the inherent limitations of our age model and refrain from discussions related to millennial-scale events.

Based on the age model, the FA24 record covers the interval between ca. 11.8 ka and ca. 0.7 ka, therefore spanning nearly the entire Holocene (Fig. 3). Sedimentation rates vary significantly between ca. 8 and 81 cm/kyr pointing to substantial shifts in local depositional processes during the examined time interval (Fig. 3). For the chronostratigraphic interpretation of our record we will be referring to the Early Holocene (11.7–8.2 ka), Middle Holocene (8.2–4.2 ka), and Late Holocene (4.2 ka to present), according to the subdivisions of (Walker et al., 2012).

4.2. XRF-CS

Core FA24 was scanned with an Avaatech (GEN-4) XRF core scanner at the Institute of Earth Sciences, Heidelberg University. The scanner is equipped with an Oxford 'Neptune 5200' 100W Rhodium X-ray source, a RAYSPEC SiriusSD 65 mm^2 Silicon Drift Detector, and a BRIGHTSPEC Topaz-X Multichannel Analyzer. Previous work has shown that XRF core scanning is a sensitive recorder of elemental variability in organic-rich sediments (Kern et al., 2019). Scanning was performed at 5 mm spatial resolution with a 5 mm downcore and 10 mm crosscore slit size, which resulted in an average temporal resolution of ca. 15 years. Prior to scanning, the core was smoothed and covered with a 4 μm thick Ultralene® X-ray transmission foil to prevent contamination and desiccation of the sediment. Excitation configuration parameters were set at 10 kV (no filter), 100 μA with a counting time of 10 s, and 30 kV (Pb-thick filter), 1000 μA with a counting time of 10 s. X-ray spectra were processed with the bAxil spectrum analysis software BrightSpec (www.brightspec.be). To avoid potential bias from variations in water content and sediment surface irregularities, elemental XRF-CS counts were normalised to the sum of all XRF-CS counts within each run.

4.3. Tetraether lipid biomarkers

Lipid biomarkers were analysed in the *Department* of Civil and Environmental Engineering and Earth Sciences at the *University of Notre Dame*. Briefly, the total lipid extracts (TLEs) were extracted from 49 freeze-dried and homogenized sediment samples (ca. 3 g dry sediment) with an accelerated solvent extractor (Dionex™ ASE) in a 9:1 dichloromethane (DCM):methanol (MeOH) (v:v) mixture. The samples have an average temporal resolution of ca. 250 years. To enhance temporal resolution during the isolated phase of the early Holocene, sampling density was increased in the lower part of the core, resulting in comparatively lower resolution in the upper sections. TLEs were then separated on aminopropyl gel columns into the neutral/polar (N/P), free fatty acid (FFA), and phospholipid fatty acid (PLFA) fractions with 2:1 DCM:2-propanol (v:v), 4% glacial acetic acid in ethyl acetate, and MeOH, respectively. The N/P fractions were subsequently separated on an alumina oxide gel column into the apolar, neutral, and polar fractions with 9:1 Hexane:DCM (v:v), 1:1 Hexane:DCM (v:v), and 1:1 DCM:MeOH (v:v), respectively. Prior to measurement, the GDGT containing polar fractions were dissolved in a 99:1 hexane: isopropanol (v:v) mixture and filtered through a 0.45 μm PTFE filter while 1 μg of C_{46} glycerol dialkyl tetraether (Huguet et al., 2006) was added as an internal standard for quantification purposes.

Samples were analysed on an Agilent 1260 Infinity II HPLC, coupled to an Agilent G6125B single quadrupole mass detector. The chromatographic method was set according to (Hopmans et al., 2016) in selected ion monitoring (SIM) mode. Two UHPLC silica columns (BEH HILIC columns, 2.1 x 150 mm, 1.7 μm; Waters) were used in series at 30° C, with a flow rate of 0.2 ml/min and a total run time of 120 min. Hexane (A) and 9:1 hexane:isopropanol (v:v) (B) were used for elution as follows: 18% of B for 25 min, followed by a linear increase up to 35% B for 25 min, and finished with a linear increase up to 100% B for 30 min. Peak areas of 1 x 10^3 and 1 x 10^7 units were defined as the lower and upper limits of quantification, respectively. Isoprenoid and branched GDGTs were identified in the mass chromatograms by their $[M+H]^+$ ions (protonated mass) at *m/z* 1292.3, 1296.3, 1298.3, 1300.3, and 1302.4 for isoGDGTs, and *m/z* 1018.0, 1020.0, 1022.0, 1032.0, 1034.0, 1036.0, and 1050.0 for brGDGTs. The internal standard C_{46} used to quantify our peak areas was detected at *m/z* 743.8. OH-isoGDGTs were identified in the mass chromatograms by the $[M+H-18]^+$ ions at *m/z* 1296.3, 1298.3, and 1300.3. brGMGTs were detected and integrated at $[M+H]^+$ ions *m/z* 1020.0 and 1034.0 and elute around 20 min after the same molecular mass brGDGTs (Fig. 4). Identification of the brGMGTs H1020a-b and H1034a-g followed (Baxter et al., 2019a, 2019b), where the suffix a-g denotes the order of elution.

4.4. GDGT-based proxy calculations

To evaluate isoGDGT compositional variations across the Red Sea basin we calculated the TEX_{86} values (Eq. 1) according to (Schouten et al., 2002).

$$TEX_{86} = (GDGT-2+GDGT-3+cren')/(GDGT-1+GDGT-2+GDGT-3+cren') \quad (1)$$

To identify the typical Red Sea-type GDGT distribution we calculated the $\%GDGT_{RS}$ (Eq. 2) proxy according to (Inglis et al., 2015). As Red Sea archaeal populations exhibit distinct membrane lipid compositions – such as a low fractional abundance of GDGT-0 relative to cren' (Trommer et al., 2009) – the $\%GDGT_{RS}$ proxy was developed to characterize this signature, with values above 30 typically indicating a modern Red Sea-type GDGT profile.

$$\%GDGT_{RS} = (100^{*}cren')/(GDGT-0+cren') \quad (2)$$

To investigate the potential producers contributing to the isoGDGT pool we calculated the f[cren'], %GDGT-0, and methane index (MI). The f(cren') ratio (Eq. 3) is calculated according to (Baxter et al., 2021b) as an indicator of the relative contributions of Group I.1a and Group I.1b Thaumarchaeota. Higher values are interpreted to indicate the

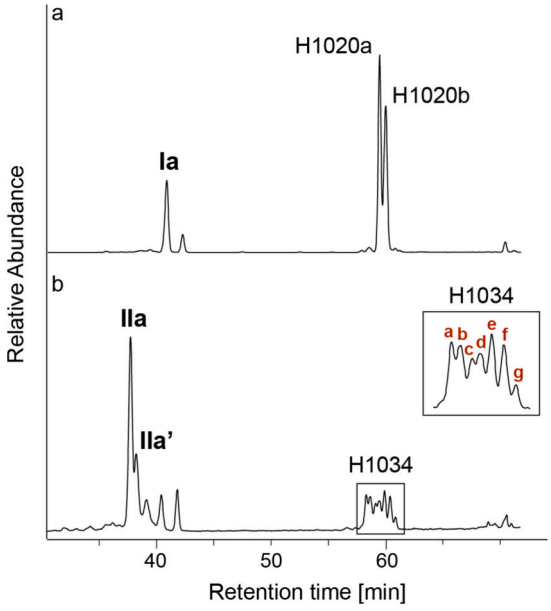

Fig. 4. Mass chromatograms for (a) *m/z* 1020.0 and (b) m/z 1034.0 obtained via UHPLC-HRMS analysis of a lipid extract from Core FA24. Both brGDGTs (with one cyclopentane ring) and brGMGTs are shown. Two isomers are detected for brGMGT 1020 (a–b), and seven isomers for brGMGT 1034 (a–g).

dominance of Group I.1b Thaumarchaeota (Baxter et al., 2021b; Sinninghe Damsté et al., 2012b). The %GDGT-0 proxy (Eq. 4) was calculated according to (Sinninghe Damsté et al., 2012a). For %GDGT-0, values over 67% may indicate a considerable methanogenic source of isoGDGT-0. The GDGT-0/crenarchaeol ratio is also interpreted in a similar way, with values over 2 indicating methanogenic sources (Blaga et al., 2009).

$$f(\text{cren}') = (\text{cren}')/((\text{cren}') + (\text{cren})) \quad (3)$$

$$\%\text{GDGT} - 0 = (100^{*}\text{GDGT} - 0)/(\text{GDGT} - 0 + \text{cren}) \quad (4)$$

The methane index (MI) (Eq. 5) is calculated to evaluate the input of methanotrophic Euryarchaeota relative to ammonia-oxidizing Thaumarchaeota (Inglis et al., 2015; Zhang et al., 2011). MI values >0.5 indicate high rates of gas-hydrate-related anaerobic oxidation of methane (AOM), while values <0.3 point to typical marine sedimentary conditions.

$$\text{MI} = (\text{GDGT} - 1 + \text{GDGT} - 2 + \text{GDGT} - 3)/(\text{GDGT} - 1 + \text{GDGT} - 2 + \text{GDGT} - 3 + \text{cren} + \text{cren}') \quad (5)$$

The GDGT-2/GDGT-3 ratio is calculated to evaluate changes in GDGT export depth according to (Taylor et al., 2013).

The abundance of hydroxylated isoprenoid GDGTs (OH-isoGDGTs) relative to the total isoGDGTs (%OH) is calculated according to (Huguet et al., 2013) (Eq. 6).

$$\%\text{OH} = (\text{OH} - 0 + \text{OH} - 1 + \text{OH} - 2)/(\text{GDGT} - 0 + \text{GDGT} - 1 + \text{GDGT} - 2 + \text{GDGT} - 3 + \text{cren} + \text{cren}' + \text{OH} - 0 + \text{OH} - 1 + \text{OH} - 2)^{*}100 \quad (6)$$

The ring indices of OH-isoGDGTs, RI-OH (Eq. 7) and RI-OH' (Eq. 8) were calculated according to (Lü et al., 2015):

$$\text{RI} - \text{OH} = (\text{OH} - 1 + 2^{*}\text{OH} - 2)/(\text{OH} - 1 + \text{OH} - 2) \quad (7)$$

$$\text{RI} - \text{OH}' = (\text{OH} - 1 + 2^{*}\text{OH} - 2)/(\text{OH} - 0 + \text{OH} - 1 + \text{OH} - 2) \quad (8)$$

The Branched and Isoprenoid Tetraether (BIT) index (Eq. 9), originally proposed by (Hopmans et al., 2004), was historically used to assess the relative contributions of terrestrially derived versus marine organic matter. High BIT values (e.g., >0.3) were interpreted as indicative of significant input from terrestrial soil bacteria, while values near 0 were associated with a purely marine signal (Weijers et al., 2006a, 2006b; Weijers et al., 2014). However, more recent studies have shown that branched GDGTs can also be produced **in situ** in marine environments (see Section 1), complicating the use of the BIT index as a straightforward terrestrial proxy.

$$\text{BIT} = (\text{Ia} + \text{IIa} + \text{IIa}' + \text{IIIa} + \text{IIIa}')/(\text{Ia} + \text{IIa} + \text{IIa}' + \text{IIIa} + \text{IIIa}' + \text{cren}) \quad (9)$$

The sources of brGDGTs are evaluated with the ΣIIIa/ ΣIIa (Xiao et al., 2016) (Eq. 10) and the $\text{Rings}_{\text{tetra}}$ indices (Sinninghe Damsté, 2016) (Eq. 11). The ΣIIIa/IIa index, an abundance ratio of hexamethylated to pentamethylated brGDGTs is based on empirical observations showing that marine environments typically exhibit higher proportions of IIIa relative to IIa, likely reflecting adaptations to higher pH and lower temperature conditions (Xiao et al., 2016). The $\#\text{Ring}_{\text{tetra}}$ index measures the degree of cyclization in tetramethylated brGDGTs and can distinguish between soil-derived and marine-derived sources, with values >0.7 indicative of a predominantly marine signal.

$$\Sigma\text{IIIa}/\Sigma\text{IIa} = (\text{IIIa} + \text{IIIa}')/(\text{IIa} + \text{IIa}') \quad (10)$$

$$\#\text{Rings}_{\text{tetra}} = (\text{Ib} + 2^{*}\text{Ic})/(\text{Ia} + \text{Ib} + \text{Ic}) \quad (11)$$

The relative abundances of tetra-, penta-, and hexa-methylated brGDGTs are calculated as the summed fractional abundances (Eqs. 12, 13, 14). Square brackets refer to the fractional abundances.

$$\Sigma\text{tetra} = [\text{Ia}] + [\text{Ib}] + [\text{Ic}] \quad (12)$$

$$\Sigma\text{penta} = [\text{IIa}] + [\text{IIb}] + [\text{IIc}] + [\text{IIa}'] + [\text{IIb}'] + [\text{IIc}'] \quad (13)$$

$$\Sigma\text{hexa} = [\text{IIIa}] + [\text{IIIa}'] \quad (14)$$

The isomerization ratio (IR_{6Me}) represents the fractional abundance of the penta- and hexa-methylated 6-methyl (6Me) brGDGTs, and is calculated to track changes in membrane compositions with respect to the methylation position on the alkyl chain (De Jonge et al., 2015) (Eq. 15). IIabc and IIIa are the 5Me brGDGTs, while IIabc' and IIIa' are the 6Me brGDGTs.

$$\text{IR}_{\text{6Me}} = (\text{IIa}' + \text{IIb}' + \text{IIc}' + \text{IIIa}')/(\text{IIa} + \text{IIb} + \text{IIc} + \text{IIIa} + \text{IIIa}' + \text{IIa}' + \text{IIa}' + \text{IIc}' + \text{IIIa}') \quad (15)$$

The summed abundance of brGMGTs relative to the abundance of all brGDGTs is calculated (Eq. 16) according to (Naafs et al., 2018).

$$\%\text{brGMGT} = (\Sigma\text{brGMGT})/(\Sigma\text{brGMGT} + \Sigma\text{brGMGT})^{*}100 \quad (16)$$

4.5. Loss on Ignition

Organic matter estimates for Core FA24 were obtained on a total of 104 samples (average temporal resolution of ca. 100 years) through sequential loss on ignition (LOI). Approximately 1 g of freeze-dried bulk sediment was dry-ashed at 550° C for 4 h in order to determine the organic matter content (LOI_{550}) (Heiri et al., 2001).

4.6. Semi-quantitative microfossil analysis

A semi-quantitative assessment of foraminiferal assemblages was performed on 63 samples with an average temporal resolution of ca. 200 years. Briefly, ca. 2 grams of dry sediment was wet sieved with distilled water at 63 μm and ultrasonically cleaned. Samples were then dry sieved at 125 μm to obtain two size fractions while the total planktic and benthic foraminifera tests were counted in both of those fractions. Planktic and benthic foraminifera were quantified as specimens per sediment gram (N/g). Benthic foraminifera were additionally grouped into epifaunal and infaunal taxa according to their microhabitat preferences (Jorissen et al., 2018; Jorissen et al., 1995). Following (Sergiou et al., 2022b), the variations between the relative abundances of epifaunal and infaunal benthic foraminifera (Epif. % - Inf. %) were used to estimate shifts in bottom-water oxygenation, with higher epifaunal dominance indicating better-ventilated conditions (Sergiou et al., 2022b; Singh et al., 2015; Verma et al., 2021).

The presence of diatoms was evaluated semi-quantitatively on the total sediment fraction (>63 μm) and was classified as follows: i) absent (0), ii) present (1), iii) abundant (2), and iv) dominant (3). Although the construction of a quantitative diatom assemblage record was beyond the scope of this study, 45 smear slides were prepared for a preliminary qualitative assessment of the downcore FA24 diatom composition. Representative samples were chosen from depths with a dominant diatom presence and analysed via a KEYENCE VHX-6000 digital microscope and scanning electron microscopy (SEM) at Heidelberg University in order to identify the dominant taxa (Fig. 7).

4.7. Statistical analysis

To evaluate the presence of distinct environmental phases within the FA24 record, k-means clustering and principal component analysis (PCA) were performed on the normalised high-resolution XRF-CS elemental data, with the optimal number of clusters determined

according to the Calinski-Harabasz criterion (Caliński and Harabasz, 1974). Both k-means clustering and PCA were performed in R v.4.2.2 (R Core Team, 2022) through the packages readxl, fpc, factoextra, ggplot2, tibble, dplyr, reshape2, ggbiplot, corrplot, and FactoMineR.

5. Results

5.1. XRF-CS elemental ratios and statistical analysis

K-means clustering applied to standardized XRF-CS elemental concentrations (Br, Ca, Cl, Fe, S, Si, Sr, Ti) identified three statistically distinct geochemical units within the FA24 record (Fig. S2.1). Cluster I spans the interval from ~11.8 to 8.7 cal. ka BP, Cluster II from 8.7 to 6.7 cal. ka BP, and Cluster III from 6.7 to 0.7 cal. ka BP. Complementing these results, Principal Component Analysis (PCA) of the same elemental dataset shows that the first two principal components (PCs) together account for 85.6% of the total variance, with PC1 alone explaining 70.4% and PC2 contributing an additional 15.2% (Fig. S2.2). The PCA biplot reveals a distinct geochemical separation: Fe, S, Ti, Ca, and Sr exhibit strong negative loadings on PC1, while Br, Cl, and Si show high positive loadings.

To interpret the palaeoenvironmental evolution of the Farasan Deep, we focus on five XRF-CS elemental ratios. The Ca/Ti ratio is employed to track fluctuations in the marine biogenic carbonate signal, as it has been previously applied in the southern Red Sea to differentiate between marine and detrital sedimentation (Paraschos et al., 2025). The Fe/Ti ratio is used as a redox-sensitive proxy to reconstruct variations in bottom-water oxygenation and ventilation near the sediment–water interface. In addition, S/Ti is included as a complementary redox indicator, interpreted to reflect sulfur accumulation related to bacterial sulfate reduction under reducing conditions. The co-variation of S/Ti with Fe/Ti supports its use as a proxy for sulfidic (euxinic) conditions and redox dynamics within the basin. Br/Ti is used to monitor variations in organic matter content (Ziegler et al., 2008), and Si/Ti to infer changes in biogenic silica input, primarily associated with diatom productivity (Brown, 2015).

Between 11.8 and 8.7 cal. ka BP, the FA24 record is characterized by uniformly low Fe/Ti, S/Ti, and Ca/Ti ratios (Fig. 5a–c), alongside elevated Br/Ti and Si/Ti values (Fig. 5d, e). From 8.7 to 6.7 cal. ka BP, all five elemental ratios exhibit marked variability, with coeval peaks observed in Fe/Ti, S/Ti, and Ca/Ti, and high-amplitude fluctuations in Br/Ti and Si/Ti (Fig. 5). Between 6.7 and 0.7 cal. ka BP, Fe/Ti, S/Ti, and Ca/Ti stabilize at persistently elevated levels, while Br/Ti and Si/Ti show a progressive decline and reach lower, stable values. Further details on elemental variability in Core FA24 are provided in Text S2 and Fig. S2.1.

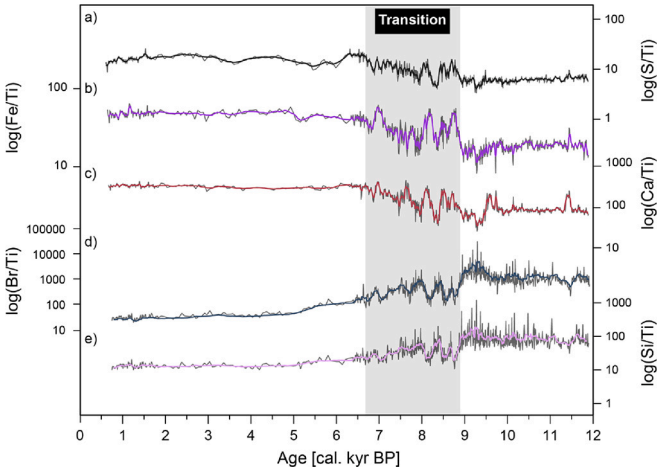

Fig. 5. Sediment geochemistry of Core FA24. Logarithmic XRF-CS elemental ratios of (a) S/Ti, (b) Fe/Ti, (c) Ca/Ti, (d) Br/Ti, and (e) Si/Ti plotted against age. The shaded gray area marks a transitional period between ca. 8.7 and 6.7 ka. Thickened coloured lines indicate a 5-point running average for each elemental ratio to highlight long-term geochemical trends.

5.2. LOI

LOI_{550} values in Core FA24 range between 10% and 26% (Fig. 6a). The interval from ca. 11.8 to 6.7 ka exhibits both elevated values and high-amplitude fluctuations, reflecting enhanced organic matter accumulation and/or preservation. At ~6.7 ka, values decrease sharply and remain consistently low through to ~0.7 ka, indicating a sustained decline in organic matter burial or preservation.

5.3. Semi-quantitative microfossil analysis

5.3.1. Foraminiferal composition

Downcore distributions of total planktic foraminifera (N/g) in both the >125 μm and <125 μm size fractions show consistent patterns (Figs S3d, S4d). From 11.8 to 8.7 ka, abundances are low, ranging from 14 to 207 N/g (Fig. 6b). After ca. 8.7 ka, planktic foraminifera exhibit a significant abundance increase and pronounced variability, ranging from 0 to 4238 N/g (Fig. 6b). Benthic foraminifera exhibit similar consistency across both size fractions (Figs S3a, S4a). Between 11.8 and 8.7 ka, total abundances remain low (0–17 N/g), including infaunal (0–16 N/g; Fig. 6d) and epifaunal specimens (0–5 N/g; Fig. 6e). From ~8.7 to 0.7 ka, total benthic abundances increase (0–643 N/g), with infaunal specimens reaching up to 413 N/g and epifaunal up to 157 N/g (Fig. 6c–e).

5.3.2. Diatom mats

The semi-quantitative diatom assessment reveals a clear three-phase structure across Core FA24 (Fig. 6h). From ca. 11.8 to 8.5 ka, the sediment is densely packed with diatom remains that occur in cohesive mat-like aggregates. These mats exhibit a high degree of preservation, including intact frustules and entangled networks of filamentous and pennate diatoms as confirmed by scanning electron microscopy (Fig. 7). The mats appear to have settled as intact flocs with inclusions of other microfossils such as foraminifera, radiolaria, and juvenile bivalves. Between ca. 8.5 and 6.5 ka, the frequency and structural coherence of diatom mats decline markedly. At ca. 6.5 ka, the mats disappear entirely, and only occasional, dispersed individual diatom frustules are observed in younger strata. Although the quantitative reconstruction of diatom assemblages is beyond the scope of this study, qualitative smear slides indicate that the assemblages are predominantly marine in origin and are dominated by centric and pennate taxa, including the chain-forming planktonic taxa *Thalassiothrix* spp. (Fig. 7c–d).

5.4. GDGTs and GDGT-based proxies

5.4.1. Distribution of iso- and brGDGTs

Concentration of the total GDGTs (branched and isoprenoid) ranges from 47 to 9671 $\mu g.g^{-1}$ TLE across the record. The GDGT pool is dominated by isoGDGTs, comprising 94.5–98.3 %, while brGDGTs contribute between 1.6 and 5.4 %. A total of 6 isoGDGT compounds are identified, including GDGT-0, GDGT-1, GDGT-2, GDGT-3, crenarchaeol and the crenarchaeol isomer (cren') (Fig. S5). Among these, GDGT-0 and crenarchaeol are the most abundant, accounting for 16–38 % and 13–53 % of the total isoGDGTs, respectively (Fig. S5a, e). Relatively smaller contributions are observed for GDGT-1 (1–17 %), GDGT-2 (7–22 %), GDGT-3 (0–10 %) and cren' (1–10 %) (Fig. S5a-f). The summed isoGDGTs concentration displays a general increase from 11.8 to 0.7 ka, structured into three distinct phases: (i) 11.8–8.7 kyr, (ii) 8.7–6.7 kyr, and (iii) 6.7–0.7 kyr (Fig. S5g). Downcore fractional abundances of the individual isoGDGTs show similar trends with the exception of GDGT-0, which shows a marked increase between 11.8 and 8.7 ka (Fig. S5).

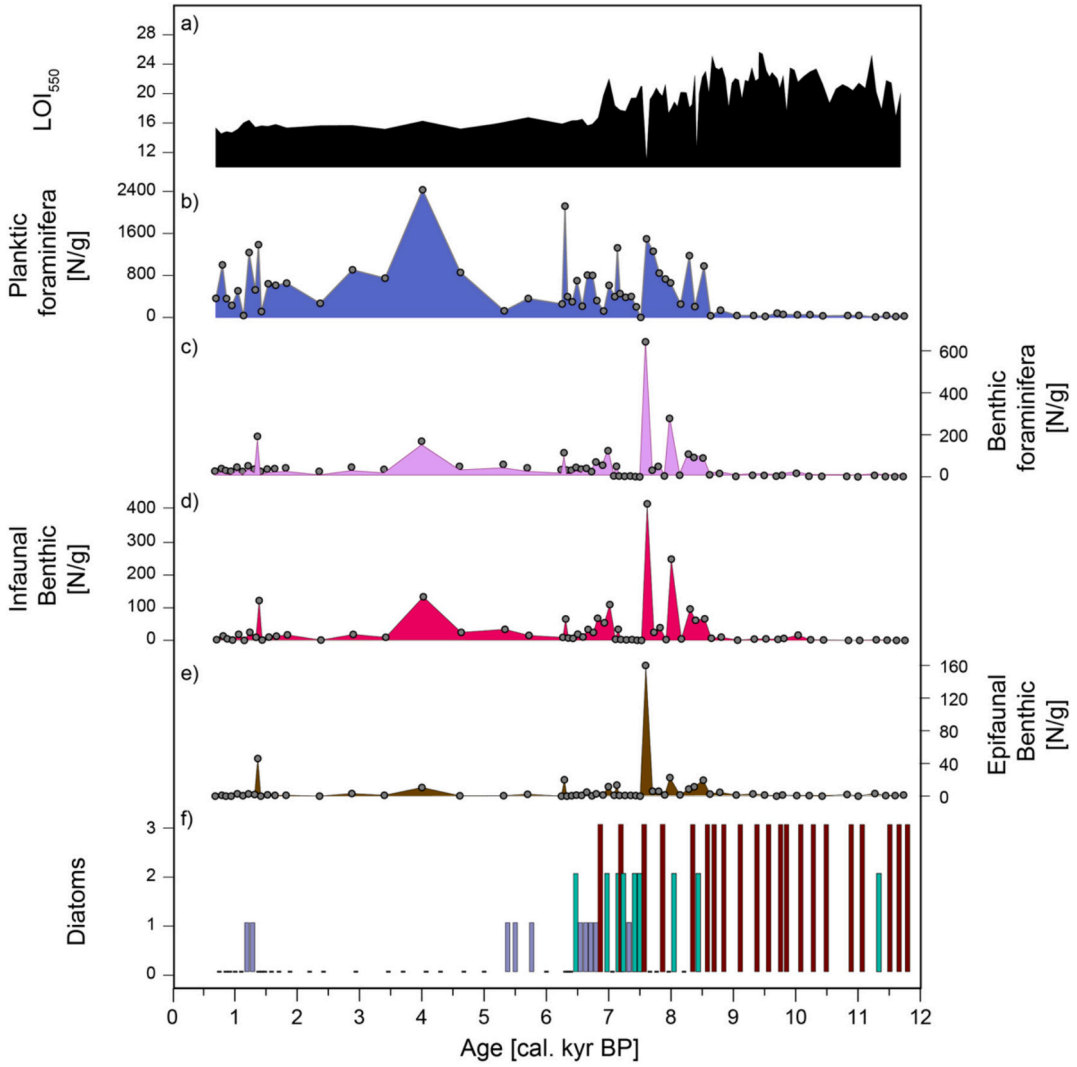

Fig. 6. Loss on ignition and semi-quantitative micropaleontological results for Core FA24. (a) LOI at 550° C, (b) planktic foraminiferal specimens (N/g), (c) benthic foraminiferal specimens (N/g), (d) infaunal benthic specimens (N/g), (e) epifaunal benthic specimens (N/g), and, (f) semi-quantitative presence of diatoms (0: absent, 1: present, 2: abundant, 3: dominant).

Three hydroxylated isoGDGTs (OH-isoGDGTs), including OH-0, OH-1 and OH-2, are detected. Total OH-isoGDGT concentrations range between 3 and 247 μg.g^{-1} TLE and exhibit an increasing trend from 11.8 to 0.7 ka, similar to that of the total isoGDGTs (Fig. S6d). OH-2 is the dominant hydroxylated isoGDGT (65–85 %), followed by OH-1 (11–32 %) and OH-0 (0–10 %) (Fig. S6a-c).

Total brGDGT concentrations range from 2 to 241 μg.g^{-1} TLE and exhibit a similar increasing trend to that of isoGDGTs and OH-isoGDGTs, delineated into the same three phases (Fig. S7l). A total of 11 brGDGTs compounds are identified, including the three tetramethylated brGDGTs (Ia, Ib, Ic), six pentamethylated brGDGTs (IIa, IIb, IIc, IIa', IIb', IIc'), and two hexamethylated brGDGTs (IIIa, IIIa') (Fig. S7). The brGDGT composition is dominated by tetramethylated brGDGTs (Σtetra), ranging between 53 and 74 % of the total brGDGT composition (Fig. S8a). Pentamethylated (Σpenta) and hexamethylated (Σhexa) brGDGTs account for 17–33 %, and 1–16%, respectively (Fig. S8b, c). Fractional abundances of the 6-methyl (6Me) brGDGTs show a distinct increase between 11.8 and 8.7 ka, especially apparent in IIa' and IIIa' (Fig. S7e, k). Cyclic brGDGTs (Ib, Ic, IIb, IIb', IIc, IIc') exhibit low fractional abundances (Fig. S7), and are dominated by the tetramethylated Ib, which ranges between 8 and 12% of the total brGDGT composition.

Branched GMGTs are detected at *m/z* 1020 and *m/z* 1034, whereas at *m/z* 1048 they were consistently below the detection limit (see Fig. 4). At *m/z* 1020, brGMGTs have two clearly defined isomers (labelled 1020a and 1020b, in order of elution), whereas *m/z* 1034 seems to have multiple and often co-eluting isomers (a-g) which we have here grouped as H1034a-g. Combined concentrations of H1020a, H1020b and H1034a–g range from 2 to 96 μg.g^{-1} TLE (Fig. S9) and show a predominantly increasing trend from 11.8 to 0.7 ka.

5.4.2. Distribution of GDGT-based proxies

The %GDGT$_{RS}$ proxy ranges between 4 and 33.6% and exhibits an increasing trend throughout the record (Fig. 8a). MI values are consistently under 0.5, with some samples below the 0.3 threshold (Fig. 8b). % GDGT-0 ranges between 25 and 49% (Fig. 8c). The GDGT-2/GDGT-3 ratio varies from 1.8 to 2.6, increasing gradually from 11.8 to 0.7 ka (Fig. 8d). The f[cren'] index ranges between 0.08 and 0.25 and remains relatively steady throughout the record (Fig. 8e). The BIT index ranges from 0.02 to 0.23, with an overall decreasing trend from 11.8 to 0.7 ka and some pronounced fluctuations during Phase II (Fig. 8f). The #Rings$_{tetra}$ index ranges from 0.30 to 0.45 and gradually declines through the record (Fig. S10a). The ΣIIIa/ΣIIa ratio varies between 0.41 and 0.93, and displays elevated values in the interval from 11.8 to 8.7 ka

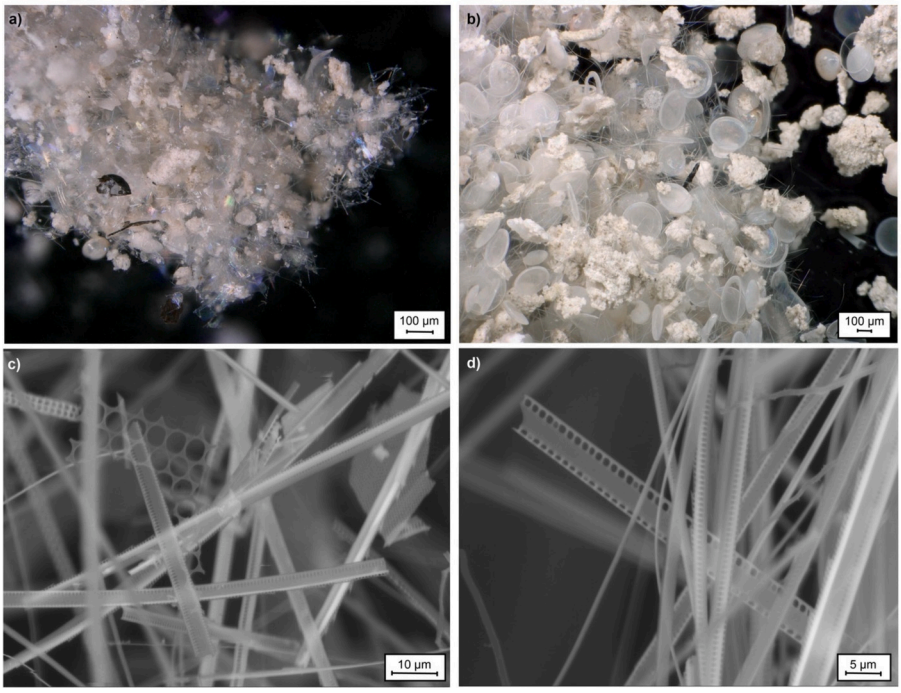

Fig. 7. Images of representative diatom deposits from the early Holocene section of Core FA24 (at 218 cm and 366 cm). (a–b) Overview of intact mat fragments showing dense, entangled networks of diatom frustules, carbonate aggregates, and bivalves. Images were taken with a KEYENCE VHX-6000 digital microscope. (c–d) Scanning electron microscopy (SEM) reveals well-preserved pennate and centric diatoms, including chain-forming taxa such as *Thalassiothrix* spp. Note the intact valve structures, visible striae, and absence of dissolution features.

(Fig. S10b). RI-OH ranges between 1.7 and 1.9, while RI-OH' between 1.5 and 1.8 (Fig. S10c, d). %OH values range between 1.3 and 4.3 % and are, on average, relatively stable throughout the record (Fig. S10e). The GDGT-0/crenarchaeol ratio ranges between 0.33 and 2.6, with the highest values observed between 11.8 and 8.7 ka (Fig. 13g). *IR_6Me values range from 0.26 to 0.65, with the highest values recorded between 11.8 and 8.7 ka, followed by a marked decline and stable lower values thereafter (Fig. 13h). The %brGMGT ranges from 13 to 61 %, peaking before ca. 8.7 ka, followed by an abrupt drop and sustained lower values through the remainder of the record (Fig. 13i).*

6. Discussion

6.1. Evaluation of iso- and br-GDGTs sources in the Farasan Deep

The Red Sea – characterized by elevated temperature and salinity, as well as biogeographical semi-isolation – hosts vertically stratified and potentially endemic microbial communities (Eder et al., 2002; Ionescu et al., 2009; Qian et al., 2011). Recent molecular evidence from the Farasan Deep specifically reveals distinct bacterial community shifts along a pronounced oxygen gradient (Klein et al., 2025), suggesting that GDGT distributions may reflect environmental restructuring and/or varying inputs from marine or terrestrial sources. Understanding GDGT source dynamics is therefore essential for interpreting the sedimentary record in this setting.

6.1.1. The Archaeal signal - isoprenoid and hydroxylated isoprenoid GDGTs

Although we lack site-specific archaeal community data for the Farasan Deep, previous studies of Red Sea surface sediments have highlighted a distinct endemic Thaumarchaeota population in the northern basin and a transitional blend of endemic and open-ocean populations (Kim et al., 2010; Kim et al., 2008) in the central and southern sections of the basin (Biton et al., 2010; Trommer et al., 2009). For example, it has been estimated that the present central Red Sea has a composition of 72% endemic and 28% open-ocean Thaumarchaeota (Trommer et al., 2011; Trommer et al., 2009). This admixture is thought to be modulated by sea-level variability and monsoon-driven exchange through the Bab al Mandab Strait, which allows for periodic incursions of the cool and nutrient-rich Gulf of Aden Intermediate Water (GAIW) up to 19–20 °N (Biton et al., 2010; Sofianos and Johns, 2007; Trommer et al., 2009a). Trommer et al. (2009) identified a biogeographic boundary near 21.5 °N (~1200 km north of the Bab al Mandab, with a salinity of 29 psu and SST of 28°C), north of which endemic Thaumarchaeota dominate. The Farasan Deep lies within this transitional zone (~ 700 km south of this boundary), where dynamic water-mass exchange with the Gulf of Aden likely drives archaeal community variability. When plotting surface sediment TEX_{86} values (Trommer et al., 2009) against distance from the Bab al Mandab strait, the modern Farasan Deep composition distinctly diverges from the Red Sea's southern sector trend (Fig. 9), reflecting its unique hydrographic setting and **a locally structured archaeal community shaped by mixed water masses.**

Non-Thaumarchaeotal isoGDGT sources, such as anaerobic methane-oxidizing archaea, appear to contribute minimally to the GDGT pool in the Farasan Deep. This is indicated by consistently low Methane Index (MI) values (all <0.5; Fig. 8b), which fall below the threshold typically associated with substantial methanotrophic input. Additional lines of evidence, such as %GDGT-0 values below 67% (Fig. 8c) and GDGT-0/crenarchaeol ratios below 2 (Fig. 13g), also suggest negligible methanogenic archaeal contribution. The dominance of crenarchaeol (Fig. S5e) further supports a predominantly Thaumarchaeotal signal (Sinninghe Damsté et al., 2002). However, the applicability of these global thresholds to the Farasan Deep remains uncertain, given its restricted, stratified hydrographic regime and the potential for endemic archaeal communities. Thus, while our results strongly point to a Thaumarchaeotal origin for isoGDGTs, localized lipid production dynamics may diverge from established patterns, emphasizing the need for complementary microbial genetic studies to validate proxy applicability in this unique marginal marine setting.

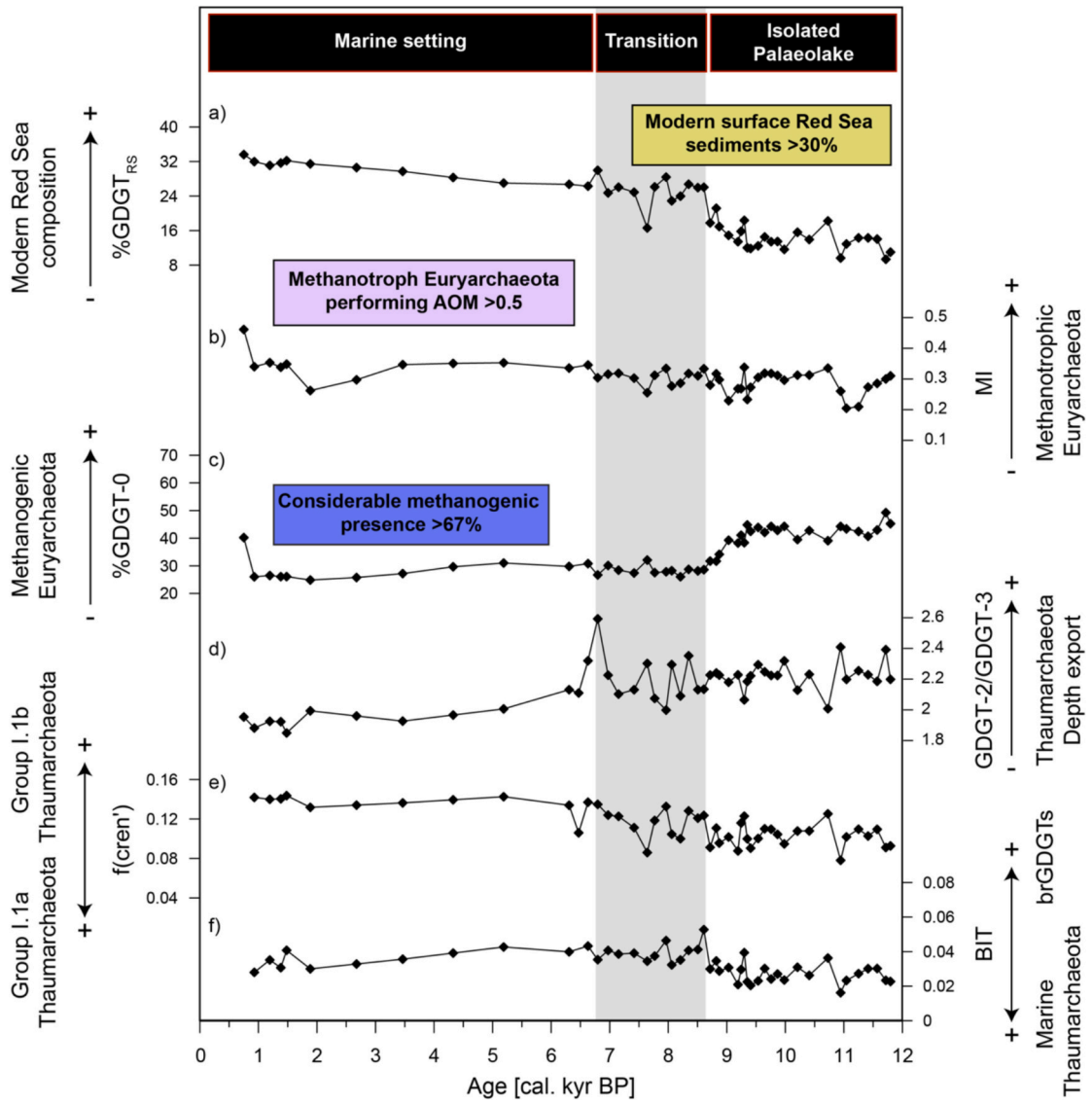

Fig. 8. GDGT-based proxies indicating tentative sources of isoprenoid and branched GDGT sources according to established thresholds. (a) %GDGT$_{RS}$ index, (b) methane index (MI), (c) %GDGT-0 proxy, (d) GDGT-2/GDGT-3 ratio, (e) f(cren') proxy, and (f) BIT index. See text for discussion.

Variations in the fractional abundance of the crenarchaeol isomer (f(cren')) have been linked to shifts in Thaumarchaeotal community structure, particularly between Group I.1a and Group I.1b. Group I.1a Thaumarchaeota, typically associated with aquatic environments, produce negligible amounts of the cren' isomer (~0–3 % of isoGDGTs), whereas Group I.1b taxa, often dominant in soil, generate significantly higher proportions (~14–29 %) (Bale et al., 2019; Kim et al., 2012; Sinninghe Damsté et al., 2012b). Consequently, elevated f(cren') values in sedimentary records have been interpreted as indicative of increased Group I.1b activity (Baxter et al., 2021a, 2021b). In the FA24 record, the f(cren') proxy exhibits pronounced variability (Fig. 8e), particularly during the early to mid-Holocene interval. These fluctuations could, in principle, reflect shifts in the relative abundance of Group I.1a versus Group I.1b Thaumarchaeota, given their distinct crenarchaeol isomer production profiles. However, without supporting molecular data, such as 16S rRNA gene surveys or metagenomic sequencing, these taxonomic inferences remain speculative.

A microbial community study of the water column overlying the Atlantis II Deep and Discovery Deep brine pools in the northern Red Sea, identified a shift from a Halobacteriales (Euryarchaeota) dominance in the upper oxygenated water layers to Desulfurococcales (Crenarchaeota) in the oxygen-depleted and sulfate-rich bottom waters (Qian et al., 2011). This vertical stratification likely reflects archaeal adaptations to changing redox and chemical conditions (Qian et al., 2011). Although these two settings are not direct analogues to the Farasan Deep, similar vertical shifts in archaeal communities - and associated variations in isoGDGT distributions - may be expected at our site.

Slight fluctuations and a long-term decline in the GDGT-2/GDGT-3 ratio, a proxy for the relative contributions of shallow- versus deep-water archaeal communities (Hurley et al., 2018; Kim et al., 2015; Taylor et al., 2013), suggest an evolving community structure in the Farasan Deep over time. Rather than solely reflecting vertical water-column changes, this trend may capture the gradual replacement of endemic palaeolake Archaea by surface open-ocean and northern Red Sea taxa introduced during Holocene sea-level rise and marine reconnection. GDGT-2/GDGT-3 values in the Farasan Deep (~2) (Fig. 8d) are substantially lower than typical values from deeper Red Sea sediments (5–11; Trommer et al., 2009; Varma et al., 2024a, 2024b), suggesting a community shaped by distinct hydrographic and ecological conditions. Similar patterns are seen in the Gulf of Aqaba, where local selection pressures, rather than geography, structure surface archaeal assemblages into distinct clusters (Ionescu et al., 2009; Teske and Sørensen,

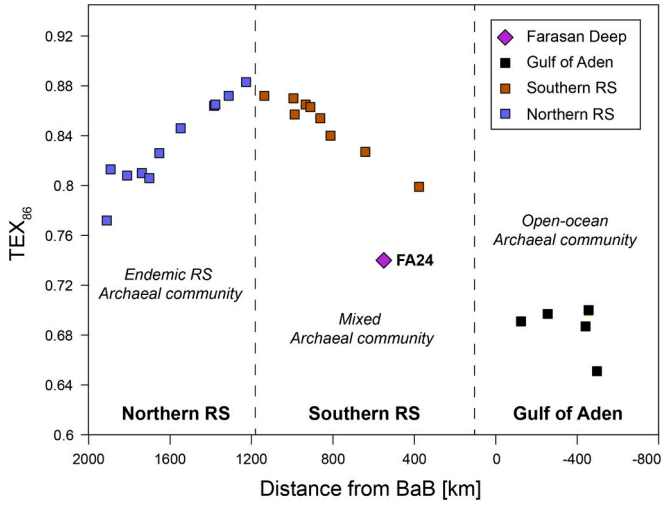

Fig. 9. TEX_{86} values of surface-sediment samples from the Red Sea plotted against their distance from the Bab al Mandab Strait, following the approach of Trommer et al. (2009). Northern Red Sea samples (orange squares) reflect the influence of endemic Thaumarchaeota communities, while Gulf of Aden samples (black squares) represent an open-ocean archaeal signature. The southern Red Sea samples (blue squares) exhibit a transitional gradient, with TEX_{86} values increasing progressively with distance from the strait, indicating the growing contribution of endemic northern Red Sea Archaea. The Farasan Deep (purple diamond, Core FA24) deviates from this regional trend, underscoring its hydrographically unique setting and the likely presence of a **composite archaeal community shaped by both Red Sea and Gulf of Aden water masses.**

2008).

The occurrence of OH-isoGDGTs in the Farasan Deep sediments, although relatively low (1.3–4.3 % of total isoGDGTs), is nevertheless notable given that previously reported values from surface sediments in the Red Sea are consistently below 1 % (Varma et al., 2024b) (Fig. 10b). The OH-isoGDGT distribution in our record is dominated by OH-2, in agreement with observations from other Red Sea localities (Varma et al., 2024b), suggesting a potentially shared source or similar environmental control on OH-isoGDGT production across the basin. The near-identical temporal trends of summed OH-isoGDGT concentrations (Fig. S6d) and total isoGDGTs (Fig. S5g) in the Farasan Deep suggest that both compound classes were produced by the same Thaumarchaeotal communities and regulated by similar environmental conditions. Varma et al. (2024a, 2024b) reported that the northern and southern Red Sea %OH, RI-OH, and RI-OH' values seem to match those for surface sediments of other tropical regions (Fig. 10b–d), thereby suggesting that perhaps the Red Sea endemic archaeal communities may not have a distinct OH-isoGDGT composition. In contrast to regional Red Sea patterns, the Farasan Deep surface sediment displays distinctly elevated %OH and RI-OH′ values relative to other surface sites across the basin, while its RI-OH values align more closely with those from the southern Red Sea (Fig. 9b–d). The elevated %OH may reflect the influence of water depth, as previous work by Varma et al. (2024b) identified a pronounced depth-dependence in %OH across Red Sea and Mediterranean sites, with deeper stations typically exhibiting lower %OH values. The discrepancy between RI-OH and RI-OH′ values in the Farasan Deep, where only RI-OH′ deviates from regional trends, stems from the inclusion of OH-0 in the RI-OH′ calculation. As such, the elevated RI-OH′ value indicates a relative depletion of OH-0 in the Farasan sediments compared to other Red Sea sediments, pointing to subtle, but potentially meaningful differences in archaeal lipid composition.

6.1.2. *The Bacterial signal - Branched GDGTs and GMGTs*

The consistently low BIT index values (<0.1) observed in the FA24 record, coupled with low brGDGT concentrations and the predominance of crenarchaeol-producing Thaumarchaeota (Sinninghe Damsté et al., 2002), indicate minimal terrestrial organic matter input, even during the early Holocene isolated palaeolake phase. These values are consistent with other Red Sea surface sediment records (Trommer et al., 2011; Trommer et al., 2009). While brGDGT scarcity is typical in offshore arid settings, recent work in shallow shelf environments suggests that in situ sedimentary production can occur under specific marine conditions, such as enhanced primary productivity and rapid particle settling (Sinninghe Damsté, 2016). This warrants consideration of marine production pathways when interpreting brGDGT provenance in the Farasan Deep.

To further assess source contributions, we applied two indices commonly used to distinguish between marine and terrestrial inputs: the **#$Ring_{tetra}$ index**, reflecting cyclization in tetramethylated brGDGTs (Sinninghe Damsté, 2016), and the **ΣIIIa/IIa ratio**, which compares hexamethylated to pentamethylated brGDGTs (Xiao et al., 2016). Various studies have reported a high degree of cyclization for in situ marine-produced tetramethylated brGDGTs (Peterse et al., 2009; Sinninghe Damsté, 2016; Zhu et al., 2011), while (Sinninghe Damsté, 2016) proposed that this increase is a cell membrane response to increasing alkalinity in the marine environment. In the FA24 record, however, #$Ring_{tetra}$ values range below the marine threshold, potentially suggesting a mixed origin involving both in situ marine production and minor terrestrial input (Fig. 11). Cyclization patterns in aquatically produced brGDGTs may also respond to environmental gradients such as salinity or temperature, or shifts in the bacterial community composition itself (Dearing Crampton-Flood et al., 2019).

Similarly, ΣIIIa/IIa values range from 0.41 to 0.94, mostly falling below the marine threshold of 0.92. This pattern mirrors observations from Red Sea surface sediments where low ΣIIIa/IIa values (0.39 ± 0.21) persist despite limited terrestrial contributions (Xiao et al., 2016), emphasizing that global thresholds may not fully apply in this region and thereby complicating the conventional use of ΣIIIa/IIa as a reliable diagnostic tool in Red Sea palaeoclimate reconstructions.

Further support for a mixed origin comes from the ternary diagram of tetra-, penta-, and hexamethylated brGDGTs (Fig. 12). The Farasan assemblage is dominated by tetramethylated brGDGTs, particularly the acyclic Ia (38–58%; Fig. S7a), consistent with tropical soils and warmer climates (Tierney et al., 2010; Weijers et al., 2007). However, the Farasan Deep samples plot between global soil datasets and Svalbard fjord sediments, commonly used as marine end-members, without clustering with either group. This intermediate position suggests a regionally unique brGDGT signature shaped by environmental specificity and potential microbial adaptation. It is worth noting that global soil datasets lack representation from hyperarid Red Sea-adjacent regions, such as northeast Africa and the Arabian Peninsula, which may explain some of the divergence.

In addition to brGDGTs, multiple isomers of brGMGTs (H1020 and H1034) were consistently detected throughout the FA24 record. These structurally distinct membrane-spanning lipids, linked by a covalent C–C bond between alkyl chains, are thought to enhance thermal stability (Naafs et al., 2018; Schouten et al., 2008). While three major compounds (H1020, H1034, H1048) are typically recognized, H1048 was not detected in the Farasan Deep, whereas a notably high degree of isomerization was detected for H1034 (up to seven distinct isomers); a complexity that has not been documented in the literature (Baxter et al., 2019a, 2019b; Baxter et al., 2021a; Hällberg et al., 2023; Kirkels et al., 2022a).

The observed decline in the %brGMGT index through time primarily reflects a disproportionate increase in brGDGTs rather than a loss of brGMGTs. Preferential degradation seems unlikely, given that both lipid classes share similar ether-bonded structures and are well-preserved in ancient sedimentary archives (Bijl et al., 2021; Liu et al., 2016). Instead, elevated %brGMGT values during the early isolated phase likely reflect enhanced production by anaerobic or facultatively anaerobic bacterial communities adapted to low-oxygen conditions, consistent with

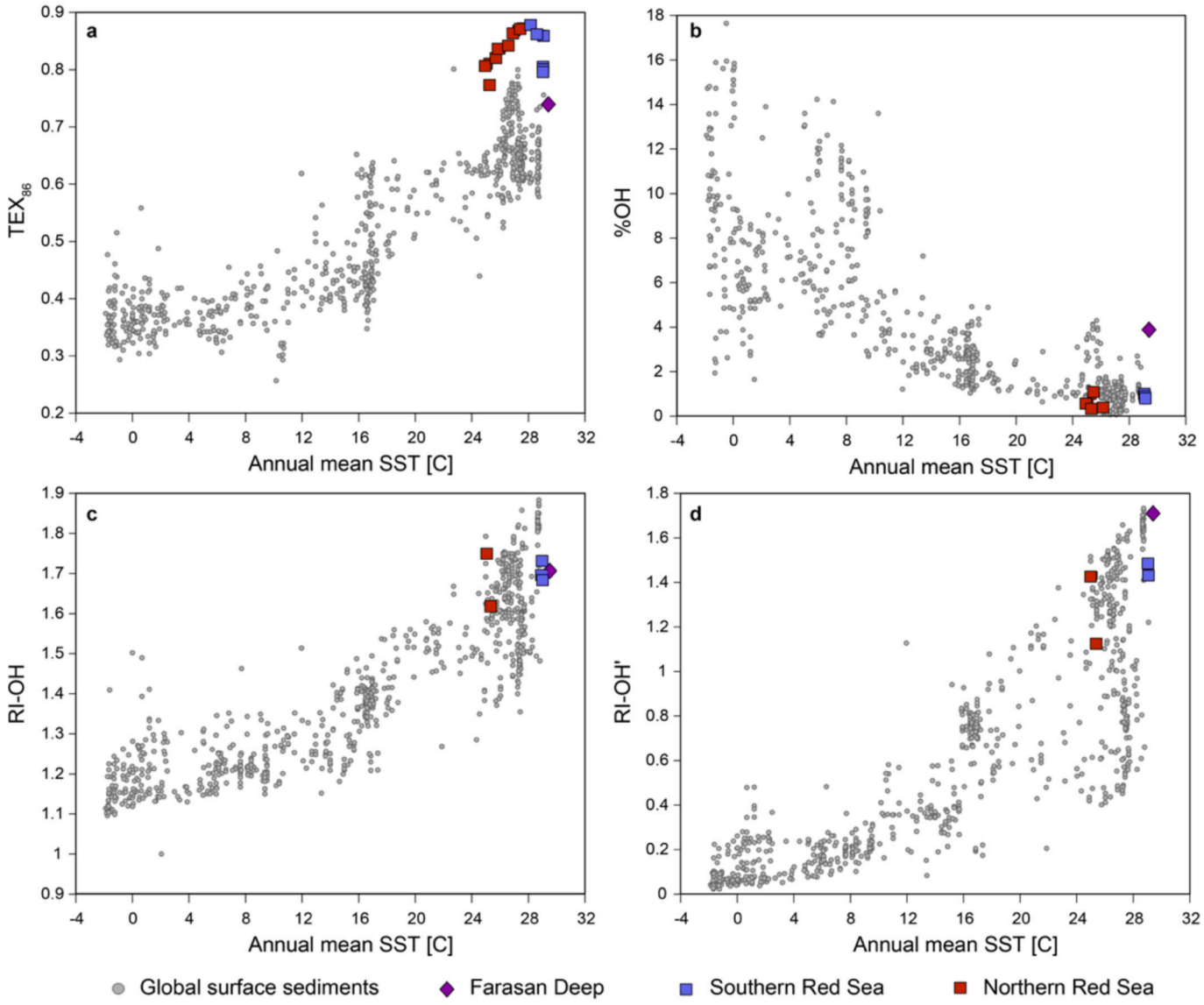

Fig. 10. Relationship between (a) TEX_{86}, (b) %OH, (c) RI-OH, and (d) RI-OH′ values and annual mean sea surface temperature (SST) in surface marine sediments. Global surface sediment data (gray circles) are taken from (Varma et al., 2024a). Surface sediment values from the northern (orange squares) and southern (blue squares) Red Sea are sourced from (Varma et al., 2024b). The Farasan Deep surface sediment is shown in purple (diamond) while the annual mean SST is from the World Ocean Atlas (2018) (Garcia et al., 2019). TEX_{86} values from the Farasan Deep are markedly lower than those of the southern Red Sea. The RI-OH Farasan value is broadly consistent with regional Red Sea patterns, whereas the %OH and RI-OH′ values are distinctly elevated, potentially reflecting local environmental controls or an archaeal community structure deviating from the typical Red Sea trends.

interpretations from both lacustrine and marine systems (Kirkels et al., 2022a; Naafs et al., 2018).

This interpretation is reinforced by modern eDNA data from the Farasan Deep water column, which document four vertically stratified bacterial communities along an oxygen gradient (Klein et al., 2025). Oxic surface waters are dominated by Alphaproteobacteria, Cyanobacteria, and Bacteroidia, while deeper, anoxic waters (125–500 m) are enriched in taxa linked to anaerobic metabolism, including Desulphobacteria, Cloacimonadia, and Omnitrophia. Notably, nitrifying Nitrospinia increase just below the oxycline (~100 m), affirming the basin's strong redox stratification. Given the persistence of this structure today, even after marine reconnection, it is reasonable to infer similar or even more pronounced microbial stratification during early Holocene isolation.

Though the precise relationship between redox conditions and brGDGT production remains uncertain, multiple studies have reported redox- and oxygen-driven shifts in brGDGT distributions (Van Bree et al., 2020; Weber et al., 2018; Wu et al., 2021; Yao et al., 2020). Experimental work has further shown that low-oxygen conditions can promote the formation of uncommon brGDGT isomers and alter methylation patterns; changes that may also influence paleotemperature proxies (Halamka et al., 2023).

Altogether, GDGT distributions in the Farasan Deep reflect a complex origin shaped by in situ marine production under varying redox and productivity regimes, and possible terrestrial input. These findings highlight the limitations of applying global GDGT thresholds in marginal or hydrographically isolated marine systems. As the connection between brGDGTs and bacterial communities remains poorly constrained in marine environments (Pan et al., 2025), detailed local water column profiling, including seasonal GDGT measurements and molecular community analyses, is essential to improve proxy resolution in settings such as the Farasan Deep (Baxter et al., 2024).

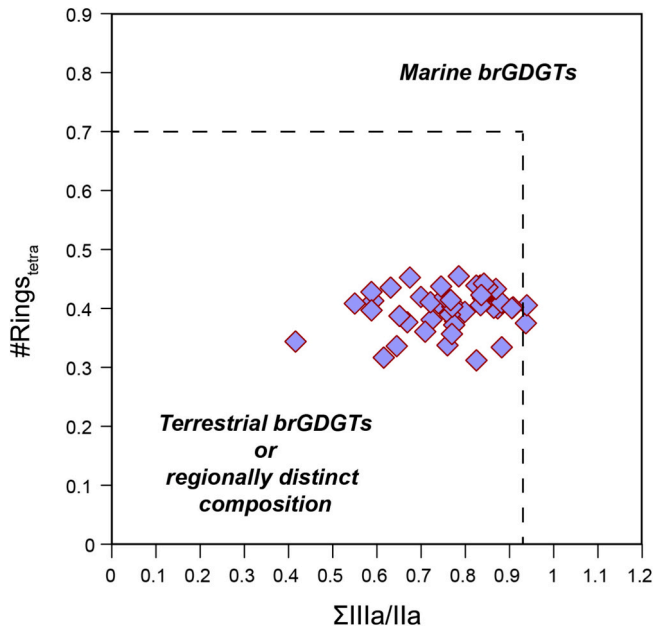

Fig. 11. Cross-plot of the ΣIIIa/IIa ratio *versus* the weighted average number of cyclopentane moieties (#Rings$_{tetra}$) in tetramethylated brGDGTs from the Farasan Deep sediments. While #Rings$_{tetra}$ values above 0.7 and ΣIIIa/ΣIIa above 0.92, indicate a predominantly marine origin of brGDGTs (Sinninghe Damsté, 2016; Xiao et al., 2016), the majority of the Farasan samples fall below the marine threshold (dashed lines), suggesting a brGDGT signal that reflects either terrestrial input or a regionally distinct community composition, rather than the global open-ocean signature seen in compiled marine datasets.

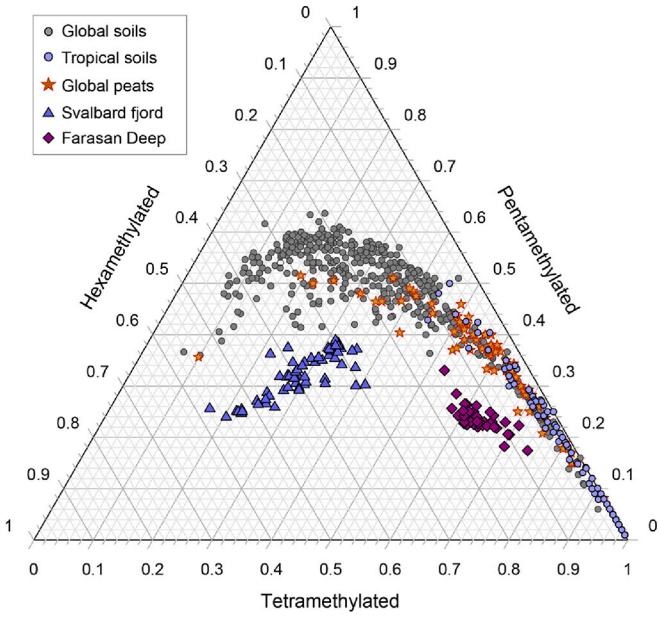

Fig. 12. Ternary diagram depicting the distribution of the tetra-, penta-, and hexa-methylated brGDGTs in the Farasan Deep sediments, the global soil compilation dataset (including tropical soils) (De Jonge et al., 2014; Dearing Crampton-Flood et al., 2020; Ding et al., 2015; Lei et al., 2016; Wang et al., 2016; Xiao et al., 2015; Yang et al., 2015), the global peat compilation dataset (Naafs et al., 2017), and the Svalbard fjord sediments (Dearing Crampton-Flood et al., 2019). The global soil dataset was compiled by (Dearing Crampton-Flood et al., 2020). As illustrated, the FA24 Farasan Deep sediments do not to plot on global soil or Svalbard fjord sediments (used as a marine end-member), although they exhibit a higher affinity to the global tropical soils.

6.2. *Palaeoenvironmental evolution of the Farasan Deep during the Holocene*

The multiproxy geochemical and micropalaeontological dataset from Core FA24 documents a three-phase evolution of the Farasan Deep during the Holocene, shaped by regional sea-level rise, basin morphology, and hydroclimatic forcing. This evolution traces the basin's transition from a hydrographically isolated palaeolake to a permanently stratified marine basin. In the following sections, each phase is examined through the lens of lipid biomarkers, XRF-CS elemental ratios, and supporting micropalaeontological observations.

6.2.1. *Phase I – an isolated palaeolake system*

Between 11.8 and ca. 8.7 ka, sedimentological and geochemical evidence from the Farasan Deep reveals a sustained interval of hydrographic isolation, marked by bottom-water anoxia and pronounced water column stratification. The dominance of fine-grained, highly flocculent sediments (Units A and B; Fig. 3, Fig. S1), coupled with elevated sedimentation rates (~75 cm/kyr) and a lack of bioturbation, reflects rapid organic accumulation under persistently low-energy, dysoxic conditions.

These conditions are consistent with reconstructions of the Red Sea relative sea level (Al-Mikhlafi et al., 2021; Grant et al., 2012), which indicate that the Farasan Deep persisted as an isolated silled basin well into the early Holocene (Fig. 1). The basin's steep bathymetry (~500 m) and the intricate topography – dotted by numerous depressions, incised valleys, and canyons (Bailey et al., 2015; Sakellariou et al., 2019) – of the adjacent carbonate shelf likely prolonged its hydrographic isolation despite ongoing postglacial transgression. Modern oceanographic observations from the Farasan Deep document persistently near-anoxic bottom waters (<2 μmol O_2 kg^{-1}; (Klein et al., 2025)), suggesting that during the early Holocene isolation similarly anoxic, if not more extreme, conditions would have prevailed.

Discrete macroplant fragments embedded within the finely laminated sequence of Unit B (Fig. S1) – tentatively identified as bark or woody tissues – exhibit exceptional preservation, consistent with strongly reducing conditions and limited microbial degradation. Although their precise botanical origin remains uncertain, the proximity of widespread mangrove and saltmarsh systems along the modern Farasan Archipelago (Alharbi, 2019) suggests that similar vegetation likely fringed the palaeolake during the early Holocene, contributing plant detritus to the basin. Evidence from characteristic mangrove-associated molluscs suggests that mangrove ecosystems were established along the Egyptian coast during the Last Interglacial, subsequently retreating during the arid conditions of the LGM, and re-expanding throughout the Red Sea basin following postglacial sea-level rise (Mayer and Beyin, 2009; Vermeersch et al., 2005).

Notably, this depositional phase unfolded within the broader framework of the African Humid Period (AHP; ca. 15–5 kyr), a climatically dynamic interval with intensified summer monsoon activity across the Arabian Peninsula that promoted widespread ecological reactivation and hydrological connectivity in regions now arid (e.g. (Foerster et al., 2012; Gasse, 2000; Tierney and DeMenocal, 2013). Reactivated wadis along the Saudi Arabian coast (Alharbi et al., 2016; Paraschos et al., 2025) may have episodically delivered freshwater and terrigenous material to the Farasan Deep – most likely during the summer monsoonal peak – briefly perturbing the water column while delivering bioavailable nutrients to the photic zone and potentially reinforcing basin stratification through freshwater capping. **These nutrient-rich terrigenous inputs, together with enhanced organic matter preservation under persistent anoxia, likely contributed to the elevated organic matter values observed during this interval.**

Hydrographic isolation, stable stratification and seasonal external forcing likely favoured episodic phytoplankton growth, particularly episodic diatom blooms. Elevated Br/Ti (Fig. 5d) and LOI values (Fig. 13a) reflect enhanced accumulation and preservation of organic

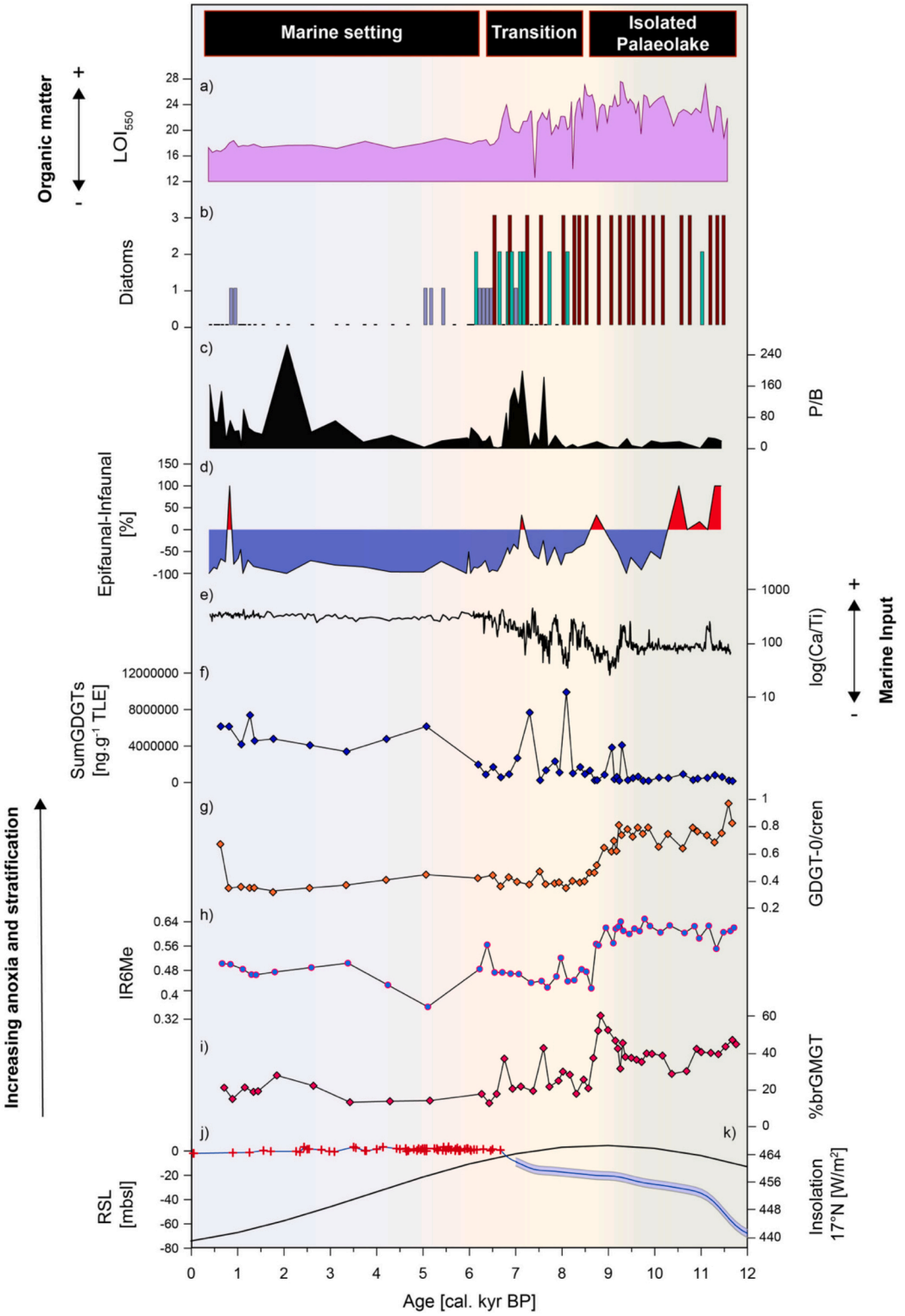

Fig. 13. Compilation of proxy records from Core FA24, in the Farasan Deep. (a) Loss on Ignition at 550 °C, (b) semi-quantitative presence of diatoms (0: absent, 1: present, 2: abundant, 3: dominant), (c) planktic-to-benthic (P/B) ratio (d) epifaunal%-infaunal% index (e) XRF-CS log(Ca/Ti) ratio (f) sum concentration of both branched and isoprenoid GDGTs normalized to the total lipid extract (TLE) (g) GDGT-0/crenarchaeol ratio (h) isomer ratio which indicates the relative contribution of 6Me versus 5Me brGDGTs, IR6Me, (i) %brGMGT index which describes the contribution of brGMGTs relative to the total brGDGT and brGMGT pool, (j) Red Sea Relative Sea Level (RSL) reconstruction, synthesized by combined data from (Al-Mikhlafi et al., 2021; Arz et al., 2007; Grant et al., 2012), and, (k) summer (June-July-August) insolation at 17 °N (Laskar et al., 2004).

matter, while high Si/Ti ratios (Fig. 5e) **and the abundance of well-preserved diatom mats (Fig. 7) point to substantial biogenic silica input and heightened productivity.** These mats form densely packed aggregates of centric and pennate taxa, particularly chain-forming species such as *Thalassiothrix* spp. (Fig. 7) and are the volumetrically most significant microfossil feature of this phase. Their formation likely reflects brief, but intense blooms in the photic zone, stimulated by episodic nutrient input and stabilized by water-column stratification that suppressed vertical mixing. Upon senescence, the diatom assemblages rapidly aggregated and sank, efficiently transferring particulate organic matter and biogenic silica to the basin floor. As evidenced by the intact frustules and lack of post-depositional dissolution, the persistence of strongly anoxic bottom waters enabled their exceptional preservation at the sediment–water interface, where they accumulated as distinct layers within the finely laminated sequence.

Both water-column turbulence, driven by external forces such as wind, tides, or upwelling, and nutrient availability are key factors in shaping phytoplankton community composition in open-ocean settings (Cullen et al., 2002; Margalef, 1978). In the modern Red Sea, however, where picophytoplankton accounts for over 90% of primary productivity (Weisse, 1989), Pearman et al. (2017) observed a notable increase in Bacillariophyceae (diatoms) in the southern sector during the fall. This seasonal rise occurred under stratified, low-turbulence conditions coinciding with elevated nutrient availability, likely introduced by the summer incursion of nutrient-rich GAIW. Under these conditions, the enhanced nutrient supply favored the proliferation of larger, fast-growing diatoms, which effectively outcompeted smaller cells (Pearman et al., 2017). By contrast, the early Holocene Farasan Deep was likely hydrographically isolated from open marine circulation, rendering direct influence from GAIW improbable. Within this context, episodic freshwater influx via wadi discharge or internally driven vertical mixing emerges as a more plausible mechanism for surface-layer nutrient delivery.

The persistent bottom-water anoxia that favored the preservation of diatom mats in the Farasan Deep also imposed severe ecological constraints on foraminiferal communities. Foraminiferal counts during this phase remain exceedingly low, yet their sporadic occurrences suggest potentially brief periods of ventilation. The low planktic-to-benthic (P/B) ratios (Fig. 13c) and the dominance of epifaunal over infaunal taxa (Fig. 13d) point to a water-column structure characterized by a shallow oxycline and steep redox gradients, with only the upper water column and upper sediment-water interface intermittently habitable. Consequently, low planktic abundances during Phase I primarily reflect restricted pelagic habitat rather than reduced surface-water productivity. This interpretation is supported by the low Ca/Ti, Fe/Ti, and S/Ti ratios (Fig. 5a–c), which reflect limited marine carbonate input, minimal authigenic sulfide formation, and a general lack of ventilation to the basin floor. However, evidence for intermittent disruptions of the prevailing redox stratification is recorded by a series of distinct light-colored layers (L1–L9; Fig. 3 and Fig. S1), which coincide with subtle enrichments in Ca/Ti and Fe/Ti (Fig. 5b, c). These deviations may reflect ventilation events, sufficient to temporarily deepen the oxycline and introduce more oxygenated conditions. Though insufficient to sustain stable faunal communities, such events offer insight into the dynamic nature of redox boundaries and their potential modulation by external forcing during this final stage of isolation.

Microbial lipid signatures in the Farasan Deep sediments further highlight the ecological distinctiveness of Phase I, from Phases II and III. The overall low concentrations of both isoprenoid and branched GDGTs (Fig. 13f) suggest lower contributions of microbial lipids to the sedimentary pool. While the scenario of increased GDGT degradation is possible, we believe that this is unlikely since the highly anoxic conditions would most likely enhance the preservation of these lipids. At the same time, GDGTs are considered to be resilient to degradation on our timescale (Schouten et al., 2013). On the contrary, these low concentrations are consistent with conditions that favored large, fast-growing eukaryotic phytoplankton, such as diatoms, over microbial loop-dominated communities (Cullen et al., 2002). As modern observations from the southern Red Sea indicate, in stratified, nutrient-enriched but low-turbulence systems, diatoms tend to outcompete smaller picoplankton, thereby reducing the relative abundance of GDGT-producing Archaea and Bacteria (Pearman et al., 2017). Since microbial community structure is tightly linked to GDGT distributions (Chen et al., 2024), these low GDGT signals likely reflect both suppressed microbial productivity and a fundamentally altered microbial assemblage. For instance, the deep, dark, and hypersaline environments of modern Red Sea brine pools, which could be functionally analogous to the early Holocene Farasan Deep, are thought to potentially harbour only heterotrophic and halotolerant microbial taxa (Qian et al., 2011). Furthermore, recent studies in stratified lakes have highlighted that the position of the oxycline in the water column strongly influences the ecological niche available to Thaumarchaeota and, thereby, the abundances and composition of the exported isoGDGT pool (Baxter et al., 2024; Baxter et al., 2021b; Zhang et al., 2016). Intense stratification during this isolated phase presumably led to the establishment of a shallow oxycline, which further limited Thaumarchaeotal blooms, while potentially facilitating the distribution of anaerobic archaea (e.g., methanogens and anaerobic methanotrophs).

In this context, the elevated GDGT-0/crenarchaeol ratio (Fig. 13g) observed during Phase I offers critical insight into the prevailing redox and archaeal community dynamics of the Farasan Deep. This index, traditionally used to infer methanogenic activity due to the preferential production of GDGT-0 by methanogenic archaea (Blaga et al., 2009; Koga et al., 1993) has also been interpreted as a signal of intensified stratification and a vertically expanded anoxic zone, particularly in lacustrine systems such as Lake Chala in Africa (Baxter et al., 2024; Baxter et al., 2021b). In a peat core from Lake Diatas in Sumatra, (Hällberg et al., 2023) identified higher GDGT-0/cren ratios in the organic rich interval of the core, suggesting anoxic conditions and methanogenesis. Although the GDGT-0/cren values in the Farasan Deep do not exceed diagnostic thresholds for active methanogenesis (see Section 5.1.1), their marked increase during this interval is nonetheless consistent with a prolonged period of suppressed deep-water ventilation and the dominance of anaerobic microbial processes. Elevated concentrations of GDGT-0 have also been documented in hypersaline environments, where they are often found in association with high levels of archaeol, suggesting a potential link to halophilic or methanogenic microbial communities (Li et al., 2016; Turich and Freeman, 2011).

High GDGT-0 concentrations in this anoxic and stratified phase further coincide with the preferential production of 6-methyl (6Me) brGDGT isomers, as reflected by increased IR6Me values; an index that captures the relative contribution of the 6-methyl to 5-methyl brGDGTS (Fig. 13h). While we do not have Farasan Deep water-column GDGT profiles, we observe some distributional similarities with other studies that have attributed these brGDGTs to in situ production (Baxter et al., 2024; Kirkels et al., 2022a; Pan et al., 2025). For example, (Kirkels et al., 2022b) attributed the combination of high GDGT-0/cren and high 6-methyl inputs to in situ production in the Godavari River, in India, during low-oxygen conditions. In Lake Chala, the 5Me and 6Me isomers seem to be distributed in spatially distinct parts of the anoxic lower water-column and subsequently the IR6Me ratio is predominantly controlled by lake water depth (Baxter et al., 2024; Van Bree et al., 2020). According to (Sinninghe Damsté, 2016), the higher primary productivity and associated organic matter fluxes of this phase could promote benthic in situ brGDGT production in the Farasan Deep. However, the possibility of a fluvial transport of brGDGTs produced in the local wadis and transferred to the Farasan Deep basin, cannot be excluded.

Finally, the very high brGMGT abundances (Fig. 13i) during this phase may also reflect preferential in situ bacterial production of GMGTs under persistently stratified and anoxic conditions. These results align with previous findings showing brGMGT in situ production in anoxic

systems such as the deep water-column and sediment of Lake Chala (Baxter et al., 2021a) and the water-saturated anoxic zone of peatlands (Naafs et al., 2018). brGMGT presence in Holocene marine sediments from the Bay of Bengal also supports a marine origin, likely from in situ production in anoxic deep waters or sediments (Kirkels et al., 2022a), reinforcing the interpretation for the Farasan Deep.

6.3. Phase II – transitional dynamics and episodic connectivity

Phase II captures an interval of hydrological reorganization, between ca.8.7 and 6.7 ka, during which the Farasan Deep began transitioning from an isolated, anoxic basin towards increased intermittent connectivity with the open southern Red Sea. This period is marked by a gradual breakdown of the stable stratification and a restructuring of biogeochemical processes, coinciding with a continued rise in regional sea level (Fig. *13*j). Sedimentologically, this phase differs from the finely laminated, flocculent textures of Phase I. *The sediments become increasingly compacted, with a clear absence of laminations and a substantial decline in sedimentation rates* (Unit C; Fig. *3* and Fig. S1). The distinct lighter-coloured layers (L10–L15) likely represent marine pulses and brief disruptions in density stratification, leading to ventilation events within the water-column (Fig. *3* and Fig. S1). Geochemically, the increased variability in Ca/Ti, Fe/Ti, and S/Ti ratios (Fig. *5*a–c) further corroborates the episodic marine influence and subsequent dynamic redox conditions. *Concurrent variability in Br/Ti and Si/Ti ratios (*Fig. *5d, e) as well as* LOI_{550} (Fig. 13a) reflects less stable surface productivity regimes, with intermittent peaks hinting at reduced but still episodic biogenic silica export.

Consistent with this geochemical signal, decreases in diatom mat formations (Fig. 13b) suggest a deterioration of the stable, diatom bloom-favoring conditions of the preceding phase. Episodic marine intrusions likely disrupted stratification in the photic zone and intermittently deepened the oxycline. Simultaneously, this phase coincided with the regional peak of the African Humid Period, when intensified precipitation could have sustained intermittent fluvial input to the Farasan Deep, **as observed in both the southern** (Paraschos et al., 2025) **and central Red Sea** (Ehrmann et al., 2024)**.** Such freshwater inflow may have diluted the marine signal while delivering pulses of nutrients to the surface waters. The resulting variability in redox and productivity proxies may thus reflect a dynamic interplay between marine incursions and terrestrial runoff, each modulating stratification, nutrient delivery, and microbial ecosystem structure in an alternating fashion.

Micropaleontological indicators also capture this ecological transition. Planktic foraminifera become increasingly abundant, marking the intermittent return of open-water connectivity and improved surface-water oxygenation (Fig. 6c and Fig. 13c). Benthic foraminifera appear in distinct pulses (Fig. 6d), with both epifaunal (Fig. 6g) and infaunal (Fig. 6f) taxa sporadically present. The alternating dominance of epifaunal *versus* infaunal groups (Fig. 13d) may reflect unstable redox conditions at the sediment–water interface. These fluctuations were likely driven by shifting oxycline depths, with alternating periods of enhanced oxygen penetration and more reducing conditions.

GDGT trends support the ecological restructuring observed during this transitional interval. The total abundance of both isoprenoid and branched GDGTs shows marked fluctuations (Fig. 13f), contrasting the suppressed levels under the low-mixing, diatom-dominated regime of Phase I. Similar patterns have been observed in Lake Chala, where a rise in GDGT concentrations coincided with the disappearance of benthic diatoms, interpreted as evidence for sustained bottom-water anoxia and the expansion of suboxic to anoxic niches favorable for aquatic GDGT production (Baxter et al., 2024). Furthermore, key redox- and source-sensitive proxies, including the GDGT-0/crenarchaeol ratio, IR6Me, and brGMGT abundances decline abruptly in our record, signaling a shift away from Archaeal and Bacterial groups adapted to low-oxygen and highly stratified conditions (Fig. 13g–i). More specifically, the noticeable IR6Me decrease (Fig. 13h) suggests a microbial shift from more 6-methyl brGDGT to a more 5-methyl brGDGT-producing community.

This transitional phase, which persisted for ca. 2 kyr, likely reflects the breakdown of persistent stratification and the onset of more dynamic photic zone conditions, with increased mixing and nutrient recycling favoring a microbial loop-dominated system, as has also been observed in the southern Red Sea during the spring months (Cullen et al., 2002; Pearman et al., 2017). The rising $\%GDGT_{RS}$ values, periodically surpassing the 30 % threshold, characteristic of modern Red Sea surface sediments (Inglis et al., 2015), further underscore a growing marine overprint and the restructuring of Archaeal niches. Pronounced variability in the GDGT-2/GDGT-3 ratio (Fig. 8d), typically used to infer Archaeal depth export (Taylor et al., 2013), potentially suggests variations in the Archaeal water-column composition resulting from fluctuating water column stratification and ventilation. Together, these patterns reflect a basin in transition: no longer a fully isolated basin, yet not a fully established marine system.

6.3.1. Phase III – Establishment of modern marine conditions

The onset of **Phase III** at ca. **6.7 ka** marks the transition of the Farasan Deep into a persistently marine basin. This shift reflects the stabilization of postglacial sea-level rise and the basin's full hydrological connection to the southern Red Sea. However, while marine conditions were clearly established, the Farasan Deep remained a **morphologically and biogeochemically distinct sub-basin**, as its hydrographic and microbial signatures continued to deviate from both global marine signals and broader regional Red Sea trends (Fig. 10).

Sedimentological evidence indicates a marked difference from the laminated, organic-rich textures of Phase I and the transitional layered sequences of Phase II that capture episodic fluctuations in water-column dynamics. The sediments of Phase III (Unit D; Fig. 3 and Fig. S1) become more homogeneous and structurally compact, devoid of lamination, reflecting a regime of stable sedimentation under persistently stratified conditions. This lithological stabilization is also mirrored in the geochemical record. **Marine and redox-sensitive elemental ratios**, including **Ca/Ti, Fe/Ti, and S/Ti (**Fig. **5a–c)**, remain consistently **elevated**, indicating persistent marine influence and a sustained suboxic to anoxic bottom-water environment. **Br/Ti and Si/Ti ratios (**Fig. **5d–e) decline and remain consistently low**, indicating reduced aquatic productivity and diminished input of biogenic silica. The **LOI profile (**Fig. **13a)** further supports this trend, showing **low and stable organic matter content,** consistent with a decrease in primary productivity and less favorable conditions for organic matter preservation.

Diatom mats (Fig. **13b), a dominant feature in earlier phases, vanish entirely,** pointing to both altered photic zone dynamics and increased degradation potential under changing redox conditions. In contrast, planktic foraminifera become generally more abundant than in preceding phases, albeit with notable fluctuations in their concentrations (Fig. 6c). These patterns nonetheless suggest a broad trend toward improved surface-water ventilation and sustained marine influence. Data from (Klein et al., 2025) show that even under modern conditions the Farasan Deep remains severely anoxic below ca. 100 m, with a sharply defined oxycline that has likely controlled the distribution and abundance of planktic communities. Meanwhile, benthic foraminifera remain comparatively sparse and are predominantly composed of infaunal species (Fig. 13d), reinforcing the interpretation of a persistently suboxic sediment–water interface despite enhanced surface exchange.

Lipid biomarker trends further underscore the ecological transition associated with Phase III. A pronounced decline in the GDGT-0/crenarchaeol ratio (Fig. 13g) signals the deepening of the oxycline, paralleling observations in stratified lacustrine environments, where such shifts mark transitions in archaeal community composition triggered by intensified water-column mixing (Baxter et al., 2024). Concurrently, the f(cren') index (Fig. 8e) stabilizes at relatively elevated values, potentially reflecting an increased contribution from

Thaumarchaeota Group I.1b (Baxter et al., 2021b). While the precise taxonomic source remains uncertain in the absence of molecular data, the trend points to a restructuring in Thaumarchaeotal niches under increasingly ventilated conditions. Meanwhile, branched lipid proxies such as the IR6Me (Fig. 13h) reflect the sustained 5-methyl brGDGT production, while the persistent low %brGMGT values (Fig. 13i) may imply that brGMGT-producing organisms are outcompeted by brGDGT-producing ones.

This restructuring is further reflected by the increase in the % $GDGT_{RS}$ index (Fig. 8a), which remains above the modern Red Sea threshold (Inglis et al., 2015), suggesting that Thaumarchaeotal communities more typical of well-mixed, oxic Red Sea environments had become ecologically dominant. However, despite this similarity to modern Red Sea %$GDGT_{RS}$ values, the Farasan Deep continues to diverge from the regional trends. Hydroxylated GDGT-derived indices such as %OH (Fig. 10b) and RI-OH' (Fig. 10d) as well as the TEX_{86} (Fig. 10a) values remain offset from both the global and existing Red Sea datasets, reinforcing the basin's persistent unique character even in its modern marine state.

In sum, Phase III marks the establishment of modern Farasan Deep conditions from ca. 6.7 ka onwards; **permanently marine, hydrographically connected, yet still biogeochemically distinct from the rest of the Red Sea basin**. While the stratification and isolation that characterized the early Holocene decreased, the Farasan Deep retained a **highly anoxic character** with a microbial ecology not fully represented in existing calibration datasets.

7. Conclusions

The Holocene evolution of the Farasan Deep reveals a prolonged and complex transition from an isolated saline palaeolake to a permanently stratified marine system, shaped by sea-level rise, climatic forcing, and basin morphology. Despite proximity to reactivated fluvial systems during the African Humid Period, the basin remained consistently saline throughout its isolated phase, underscoring the persistence of restricted exchange and evaporative dominance in marginal marine depressions.

The atypical GDGT distributions, distinct archaeal signals, and diatom-rich intervals highlight the influence of redox stratification, microbial restructuring, and internal nutrient cycling on lipid biomarker production and preservation. These findings underscore the need for caution when applying conventional GDGT-based paleoclimate proxies in marginal marine or hydrographically restricted settings, where microbial community shifts and environmental isolation can significantly alter GDGT production and export. Proxy thresholds established in fully marine or lacustrine systems may not directly apply to such transitional environments, while to improve the applicability of these proxies, future research should combine seasonal water column sampling with molecular microbial analyses (e.g., 16S rRNA sequencing, metagenomics) to identify GDGT-producing taxa and refine the applicability of GDGT-based proxies in marginal marine systems like the Farasan Deep.

Beyond the regional framework, the Farasan Deep offers a globally relevant analogue for understanding stratification feedbacks, redox-sensitive carbon cycling, and microbial lipid responses in semi-enclosed systems. Its depositional archive serves as a valuable template for evaluating biogeochemical evolution in submerged coastal basins and contributes to the growing recognition of their palaeoenvironmental and geoarchaeological significance. These results emphasize the need for integrative multiproxy approaches and microbial characterization to refine climate reconstructions and assess early human–environment interactions in now-submerged landscapes.

CRediT authorship contribution statement

Francesca Paraschos: Writing – review & editing, Writing – original draft, Visualization, Methodology, Investigation, Funding acquisition, Formal analysis, Data curation, Conceptualization. **Melissa A. Berke:** Writing – review & editing, Writing – original draft, Investigation. **Andreas Koutsodendris:** Writing – review & editing, Writing – original draft, Methodology, Investigation. **Oliver Friedrich:** Writing – review & editing, Writing – original draft, Investigation. **Spyros Sergiou:** Writing – review & editing, Methodology. **Maria Geraga:** Writing – review & editing, Supervision. **Helen Kaberi:** Writing – review & editing, Supervision. **Ross Williams:** Methodology. **Geoffrey Bailey:** Writing – review & editing, Writing – original draft, Supervision, Resources, Project administration, Funding acquisition, Conceptualization. **Jörg Pross:** Writing – review & editing, Writing – original draft, Resources. **Dimitris Sakellariou:** Writing – review & editing, Writing – original draft, Supervision, Resources, Project administration, Funding acquisition, Conceptualization.

Funding

This research was funded by the European Research Council through ERC Advanced Grant 269586 "DISPERSE: Dynamic Landscapes, Coastal Environments and Human Dispersals" under the 'Ideas' Specific Programme of the Seventh Framework Programme. F.P. acknowledges funding by the Hellenic Center for Marine Research (HCMR) during the full course of this research work, the International Union for Quaternary Research (INQUA) Fellowship Program for International Mobility (2023), and the Organic Geochemistry Elsevier Research Scholarship (2023).

Declaration of competing interest

We declare that this manuscript has been approved for submission by all authors; that it is being submitted solely for consideration by *Global and Planetary Change*; and that all data presented are unpublished. We have no conflicts of interest to disclose.

Acknowledgments

We would like to acknowledge the captain and crew of the R/V 'AEGAEO' for their continuous assistance during the 2021 research cruise. We would also like to thank the Saudi Commission for Tourism and National Heritage (SCTH), and the Department of General Survey of the Ministry of Defense for fieldwork permissions. George Krokos, Karl Meier, Daniela Müller, Dimitris Velaoras, and Mirko A. Uy are thanked for fruitful discussions. Steve Bohaty is thanked for diatom identification, and Pavlos Coulondre is thanked for his help with foraminifera counting. Vivi Drakopoulou, Kayla Hollister, Laurin S. Kolb, and Sönke Szidat are thanked for technical support. This is DISPERSE contribution no. 68.

Appendix A. Supplementary data

Supplementary data to this article can be found online at https://doi.org/10.1016/j.gloplacha.2025.105176.

Data availability

All datasets presented in this study can be accessed via the following link: https://doi.org/10.17882/109645.

References

Alharbi, S.A., 2019. A Phylogenetic Assessment of the Affinities of the Farasan Islands Flora. PhD Thesis. School of Biological Sciences, University of Reading.

Alharbi, O.A., Williams, A.T., Phillips, M.R., Thomas, T., 2016. Textural characteristics of sediments along the southern Red Sea coastal areas, Saudi Arabia. Arab. J. Geosci. 9, 735. https://doi.org/10.1007/s12517-016-2741-y.

Al-Mikhlafi, A.S., Hibbert, F.D., Edwards, L.R., Cheng, H., 2021. Holocene relative sea-level changes and coastal evolution along the coastlines of Kamaran Island and As-Salif Peninsula, Yemen, southern Red Sea. Quat. Sci. Rev. 252, 106719. https://doi.org/10.1016/j.quascirev.2020.106719.

Arz, H.W., Lamy, F., Pätzold, J., Müller, P.J., Prins, M., 2003. Mediterranean moisture source for an early-Holocene humid period in the northern Red Sea. Science 300, 118–121. https://doi.org/10.1126/science.1080325.

Arz, H.W., Lamy, F., Ganopolski, A., Nowaczyk, N., Pätzold, J., 2007. Dominant Northern Hemisphere climate control over millennial-scale glacial sea-level variability. Quat. Sci. Rev. 26, 312–321. https://doi.org/10.1016/j.quascirev.2006.07.016.

Bailey, G., 2015. The Evolution of the Red Sea as a Human Habitat During the Quaternary Period. In: Rasul, N., Stewart, I. (Eds.), The Red Sea. Springer Earth System Sciences. Springer, Berlin, Heidelberg. https://doi.org/10.1007/978-3-662-45201-1_34.

Bailey, G., Cawthra, H.C., 2023. The significance of sea-level change and ancient submerged landscapes in human dispersal and development: A geoarchaeological perspective. Oceanologia 65, 50–70. https://doi.org/10.1016/j.oceano.2021.10.002.

Bailey, G.N., Devès, M.H., Inglis, R.H., Meredith-Williams, M.G., Momber, G., Sakellariou, D., Sinclair, A.G.M., Rousakis, G., Al Ghamdi, S., Alsharekh, A.M., 2015. Blue Arabia: Palaeolithic and underwater survey in SW Saudi Arabia and the role of coasts in Pleistocene dispersals. Quat. Int. 382, 42–57. https://doi.org/10.1016/j.quaint.2015.01.002.

Bailey, G.N., Meredith-Williams, M., Alsharekh, A.M., Hausmann, N., 2019. The archaeology of Pleistocene coastal environments and human dispersal in the Red Sea: Insights from the Farasan Islands. In: Rasul, N.M.A., Stewart, I.C.F. (Eds.), Geological Setting, Palaeoenvironment and Archaeology of the Red Sea. Springer, Berlin Heidelberg, pp. 587–608. https://doi.org/10.1007/978-3-319-99408-6_26.

Bailey, G., Galanidou, N., Peeters, H., Jöns, H., Mennenga, M., 2020. The archaeology of europe's drowned landscapes: introduction and overview. Coastal Research Library 35, 1–23. https://doi.org/10.1007/978-3-030-37367-2_1.

Bale, N.J., Palatinszky, M., Rijpstra, W.I.C., Herbold, C.W., Wagner, M., Damsté, J.S.S., 2019. Membrane lipid composition of the moderately thermophilic ammonia-oxidizing archaeon "Candidatus Nitrosotenuis uzonensis" at different growth temperatures. Appl. Environ. Microbiol. 85 (20), e01332-19. https://doi.org/10.1128/AEM.01332-19.

Bantan, R.A., 1999. Geology and sedimentary environments of Farasan Bank (Saudi Arabia) southern Red Sea: A combined remote sensing and field study. PhD thesis,. University of London Royal Holloway, UK.

Baxter, Allix J., Hopmans, E.C., Russell, J.M., Sinninghe Damsté, J.S., 2019a. Bacterial GMGTs in East African lake sediments: Their potential as palaeotemperature indicators. Geochim. Cosmochim. Acta 259, 155–169. https://doi.org/10.1016/j.gca.2019.05.039.

Baxter, A.J., Hopmans, E.C., Russell, J.M., Van Bree, L.G.J., Peterse, F., Verschuren, D., Sinninghe Damsté, J.S., 2019b. Bacterial GMGTs in East African lakes: Sources and their potential as paleotemperature indicators. 29th International Meeting on Organic Geochemistry. IMOG 2019, 6–7. https://doi.org/10.3997/2214-4609.201902873.

Baxter, A.J., Peterse, F., Verschuren, D., Sinninghe Damsté, J.S., 2021a. Anoxic in situ production of bacterial GMGTs in the water column and surficial bottom sediments of a meromictic tropical crater lake: Implications for lake paleothermometry. Geochim. Cosmochim. Acta 306, 171–188. https://doi.org/10.1016/j.gca.2021.05.015.

Baxter, A.J., van Bree, L.G.J., Peterse, F., Hopmans, E.C., Villanueva, L., Verschuren, D., Sinninghe Damsté, J.S., 2021b. Seasonal and multi-annual variation in the abundance of isoprenoid GDGT membrane lipids and their producers in the water column of a meromictic equatorial crater lake (Lake Chala, East Africa). Quat. Sci. Rev. 273, 107263. https://doi.org/10.1016/j.quascirev.2021.107263.

Baxter, A.J., Peterse, F., Verschuren, D., Maitituerdi, A., Waldmann, N., Sinninghe Damsté, J.S., 2024. Disentangling influences of climate variability and lake-system evolution on climate proxies derived from isoprenoid and branched glycerol dialkyl glycerol tetraethers (GDGTs): The 250 kyr Lake Chala record. Biogeosciences 21, 2877–2908. https://doi.org/10.5194/bg-21-2877-2024.

Bijl, P.K., Frieling, J., Cramwinckel, M.J., Boschman, C., Sluijs, A., Peterse, F., 2021. Maastrichtian-Rupelian paleoclimates in the southwest Pacific - A critical re-evaluation of biomarker paleothermometry and dinoflagellate cyst paleoecology at Ocean Drilling Program Site 1172. Clim. Past 17, 2393–2425. https://doi.org/10.5194/cp-17-2393-2021.

Biton, E., Gildor, H., Peltier, W.R., 2008. Red Sea during the Last Glacial Maximum: Implications for sea level reconstruction. Paleoceanography 23, PA1214. https://doi.org/10.1029/2007PA001431.

Biton, E., Gildor, H., Trommer, G., Siccha, M., Kucera, M., Van Der Meer, M.T.J., Schouten, S., 2010. Sensitivity of Red Sea circulation to monsoonal variability during the Holocene: An integrated data and modeling study. Paleoceanography 25, 1–16. https://doi.org/10.1029/2009PA001876.

Blaauw, M., Christen, J.A., 2011a. Bacon Manual v 2.3.9.1, 1–15.

Blaauw, Maarten, Christen, J.A., 2011b. Flexible paleoclimate age-depth models using an autoregressive gamma process. Bayesian Anal. 6, 457–474. https://doi.org/10.1214/11-ba618.

Blaga, C.I., Reichart, G.-J., Heiri, O., Sinninghe Damsté, J.S., 2009. Tetraether membrane lipid distributions in water-column particulate matter and sediments: a study of 47 European lakes along a north–south transect. J. Paleolimnol. 41, 523–540.

Bouilloux, A., Valet, J.P., Bassinot, F., Joron, J.L., Dewilde, F., Blanc-Valleron, M.M., Moreno, E., 2013. Influence of seawater exchanges across the Bab-el-Mandeb Strait on sedimentation in the Southern Red Sea during the last 60 ka. Paleoceanography 28, 675–687. https://doi.org/10.1002/2013PA002544.

Brown, E.T., 2015. Estimation of Biogenic Silica Concentrations Using Scanning XRF: Insights from Studies of Lake Malawi Sediments BT- Micro-XRF Studies of Sediment Cores: Applications of a non-destructive tool for the environmental sciences. In: Rothwell, R.G. (Ed.), Croudace, I.W. Springer Netherlands, Dordrecht, pp. 267–277. https://doi.org/10.1007/978-94-017-9849-5_9.

Caliński, T., Harabasz, J., 1974. A Dendrite Method Foe Cluster Analysis. Communications in Statistics 3, 1–27. https://doi.org/10.1080/03610927408827101.

Chen, Y., Li, J., Chen, S., Xiao, W., Zheng, F., Cheng, Z., Zhang, C., 2024. Potential influence of bacterial community structure on the distribution of brGDGTs in surface sediments from Yangtze River Estuary to East China Sea. Chem. Geol. 647, 121934. https://doi.org/10.1016/j.chemgeo.2024.121934.

Churchill, J.H., Bower, A.S., McCorkle, D.C., Abualnaja, Y., 2015. The transport of nutrient-rich Indian ocean water through the red sea and into coastal reef systems. J. Mar. Res. 72, 165–181. https://doi.org/10.1357/002224014814901994.

Cullen, J.J., Franks, P.J.S., Karl, D.M., Longhurst, A., 2002. Physical influences on marine ecosystem dynamics. In: Robinson, Allan R., McCarthy, James J., Rothschild, Brian J. (Eds.), The Sea, Volume 12. John Wiley & Sons, Inc, New York.

Damsté, J.S.S., Hopmans, E.C., Pancost, R.D., Schouten, S., Geenevasen, J.A.J., 2000. Newly discovered non-isoprenoid glycerol dialkyl glycerol tetraether lipids in sediments. Chem. Commun. 1683–1684. https://doi.org/10.1039/B004517I.

De Jonge, C., Hopmans, E.C., Zell, C.I., Kim, J.H., Schouten, S., Sinninghe Damsté, J.S., 2014. Occurrence and abundance of 6-methyl branched glycerol dialkyl glycerol tetraethers in soils: Implications for palaeoclimate reconstruction. Geochim. Cosmochim. Acta 141, 97–112. https://doi.org/10.1016/j.gca.2014.06.013.

De Jonge, C., Stadnitskaia, A., Hopmans, E.C., Cherkashov, G., Fedotov, A., Streletskaya, I.D., Vasiliev, A.A., Sinninghe Damsté, J.S., 2015. Drastic changes in the distribution of branched tetraether lipids in suspended matter and sediments from the Yenisei River and Kara Sea (Siberia): Implications for the use of brGDGT-based proxies in coastal marine sediments. Geochim. Cosmochim. Acta 165, 200–225. https://doi.org/10.1016/j.gca.2015.05.044.

De Jonge, C., Stadnitskaia, A., Cherkashov, G., Sinninghe Damsté, J.S., 2016. Branched glycerol dialkyl glycerol tetraethers and crenarchaeol record post-glacial sea level rise and shift in source of terrigenous brGDGTs in the Kara Sea (Arctic Ocean). Org. Geochem. 92, 42–54. https://doi.org/10.1016/j.orggeochem.2015.11.009.

De Rosa, M., Gambacorta, A., 1988. The lipids of archaebacteria. Prog. Lipid Res. 27, 153–175. https://doi.org/10.1016/0163-7827(88)90011-2.

Dearing Crampton-Flood, E., Peterse, F., Sinninghe Damsté, J.S., 2019. Production of branched tetraethers in the marine realm: Svalbard fjord sediments revisited. Org. Geochem. 138, 103907. https://doi.org/10.1016/j.orggeochem.2019.103907.

Dearing Crampton-Flood, E., Tierney, J.E., Peterse, F., Kirkels, F.M.S.A., Sinninghe Damsté, J.S., 2020. BayMBT: A Bayesian calibration model for branched glycerol dialkyl glycerol tetraethers in soils and peats. Geochim. Cosmochim. Acta 268, 142–159. https://doi.org/10.1016/j.gca.2019.09.043.

Ding, S., Xu, Y., Wang, Y., He, Y., Hou, J., Chen, L., He, J.S., 2015. Distribution of branched glycerol dialkyl glycerol tetraethers in surface soils of the Qinghai-Tibetan Plateau: Implications of brGDGTs-based proxies in cold and dry regions. Biogeosciences 12, 3141–3151. https://doi.org/10.5194/bg-12-3141-2015.

Edelman-Furstenberg, Y., Scherbacher, M., Hemleben, C., Almogi-Labin, A., 2001. Deep-sea benthic foraminifera from the central Red Sea. J. Foraminifer. Res. 31, 48–59. https://doi.org/10.2113/0310048.

Eder, W., Schmidt, M., Koch, M., Garbe-Schönberg, D., Huber, R., 2002. Prokaryotic phylogenetic diversity and corresponding geochemical data of the brine-seawater interface of the Shaban Deep, Red Sea. Environ. Microbiol. 4, 758–763. https://doi.org/10.1046/j.1462-2920.2002.00351.x.

Ehrmann, W., Wilson, P.A., Arz, H.W., Schulz, H., Schmiedl, G., 2024. Monsoon-driven changes in aeolian and fluvial sediment input to the central Red Sea recorded throughout the last 200000 years. Clim. Past 20, 37–52. https://doi.org/10.5194/cp-20-37-2024.

Faure, H., Walter, R.C., Grant, D.R., 2002. The coastal oasis: Ice age springs on emerged continental shelves. Glob. Planet. Chang. 33, 47–56. https://doi.org/10.1016/S0921-8181(02)00060-7.

Flemming Nicholas, C., Harff, J., Moura, D., Burgess, A., Bailey, G.N., 2017. Submerged Landscapes of the European Continental Shelf. Quaternary Paleoenvironments. Wiley-Blackwell, Submerged Landscapes of the European Continental Shelf. https://doi.org/10.1002/9781118927823.

Foerster, V., Junginger, A., Langkamp, O., Gebru, T., Asrat, A., Umer, M., Lamb, H.F., Wennrich, V., Rethemeyer, J., Nowaczyk, N., Trauth, M.H., Schaebitz, F., 2012. Climatic change recorded in the sediments of the Chew Bahir basin, southern Ethiopia, during the last 45,000 years. Quat. Int. 274, 25–37. https://doi.org/10.1016/j.quaint.2012.06.028.

Fuhrman, J.A., Mccallum, K., Davis, A.A., 1992. Novel major archaebacterial group from marine plankton. Nature 356, 148–149. https://doi.org/10.1038/356148a0.

Garcia, H.E., Boyer, T.P., Baranova, O.K., Locarnini, R.A., Mishonov, A.V., Grodsky, A., Paver, C.R., Weathers, K.W., Smolyar, I.V., Reagan, J.R., Seidov, D., Zweng, M.M., 2019. World Ocean Atlas 2018.

Gasse, F., 2000. Hydrological changes in the African tropics since the Last Glacial Maximum. Quat. Sci. Rev. 19, 189–211. https://doi.org/10.1016/S0277-3791(99)00061-X.

Grant, K.M., Rohling, E.J., Bar-Matthews, M., Ayalon, A., Medina-Elizalde, M., Ramsey, C.B., Satow, C., Roberts, A.P., 2012. Rapid coupling between ice volume and polar temperature over the past 150,000 years. Nature 491, 744–747. https://doi.org/10.1038/nature11593.

Grant, K.M., Rohling, E.J., Ramsey, C.B., Cheng, H., Edwards, R.L., Florindo, F., Heslop, D., Marra, F., Roberts, A.P., Tamisiea, M.E., Williams, F., 2014. Sea-level variability over five glacial cycles. Nat. Commun. 5, 5076. https://doi.org/10.1038/ncomms6076.

Halamka, T.A., Raberg, J.H., McFarlin, J.M., Younkin, A.D., Mulligan, C., Liu, X.L., Kopf, S.H., 2023. Production of diverse brGDGTs by Acidobacterium Solibacter

usitatus in response to temperature, pH, and O2 provides a culturing perspective on brGDGT proxies and biosynthesis. Geobiology. https://doi.org/10.1111/gbi.12525.
Hale, J.C., Benjamin, J., Woo, K., Astrup, P.M., McCarthy, J., Hale, N., Stankiewicz, F., Wiseman, C., Skriver, C., Garrison, E., Ulm, S., Bailey, G., 2021. Submerged landscapes, marine transgression and underwater shell middens: Comparative analysis of site formation and taphonomy in Europe and North America. Quat. Sci. Rev. 258, 106867. https://doi.org/10.1016/j.quascirev.2021.106867.
Hällberg, P.L., Schenk, F., Jarne-Bueno, G., Schankat, Y., Zhang, Q., Rifai, H., Phua, M., Smittenberg, R.H., 2023. Branched GDGT source shift identification allows improved reconstruction of an 8,000-year warming trend on Sumatra. Org. Geochem. 186, 104702. https://doi.org/10.1016/j.orggeochem.2023.104702.
Heaton, T.J., Köhler, P., Butzin, M., Bard, E., Reimer, R.W., Austin, W.E.N., Bronk Ramsey, C., Grootes, P.M., Hughen, K.A., Kromer, B., Reimer, P.J., Adkins, J., Burke, A., Cook, M.S., Olsen, J., Skinner, L.C., 2020. Marine20-the marine radiocarbon age calibration curve (0-55,000 cal BP) Enhanced Reader.pdf. Radiocarbon 62, 779–820. https://doi.org/10.1017/RDC.2020.68.
Heiri, O., Lotter, A., Lemcke, Gerry, 2001. Loss on Ignition as a method for estimating organic and carbonate content in sediments: Reproducibility and comparability of results. J. Paleolimnol. 25, 101–110. https://doi.org/10.1023/A.
Hopmans, E.C., Weijers, J.W.H., Schefuß, E., Herfort, L., Sinninghe Damsté, J.S., Schouten, S., 2004. A novel proxy for terrestrial organic matter in sediments based on branched and isoprenoid tetraether lipids. Earth Planet. Sci. Lett. 224, 107–116. https://doi.org/10.1016/j.epsl.2004.05.012.
Hopmans, E.C., Schouten, S., Sinninghe Damsté, J.S., 2016. The effect of improved chromatography on GDGT-based palaeoproxies. Org. Geochem. 93, 1–6. https://doi.org/10.1016/j.orggeochem.2015.12.006.
Huguet, C., Hopmans, E.C., Febo-Ayala, W., Thompson, D.H., Sinninghe Damsté, J.S., Schouten, S., 2006. An improved method to determine the absolute abundance of glycerol dibiphytanyl glycerol tetraether lipids. Org. Geochem. 37, 1036–1041. https://doi.org/10.1016/j.orggeochem.2006.05.008.
Huguet, C., Fietz, S., Rosell-Melé, A., 2013. Global distribution patterns of hydroxy glycerol dialkyl glycerol tetraethers. Org. Geochem. 57, 107–118. https://doi.org/10.1016/j.orggeochem.2013.01.010.
Hurley, S.J., Lipp, J.S., Close, H.G., Hinrichs, K.U., Pearson, A., 2018. Distribution and export of isoprenoid tetraether lipids in suspended particulate matter from the water column of the Western Atlantic Ocean. Org. Geochem. 116, 90–102. https://doi.org/10.1016/j.orggeochem.2017.11.010.
Inglis, G.N., Farnsworth, A., Lunt, D.J., Foster, G.L., Hollis, C.J., Pagani, M., Jardine, P.E., Pearson, P.N., Markwick, P., Galsworthy, A.M.J., 2015. Descent toward the Icehouse: Eocene sea surface cooling inferred from GDGT distributions. Paleoceanography 30, 1000–1020. https://doi.org/10.1002/2014PA002723.
Ionescu, D., Penno, S., Haimovich, M., Rihtman, B., Goodwin, A., Schwartz, D., Hazanov, L., Chernihovsky, M., Post, A.F., Oren, A., 2009. Archaea in the Gulf of Aqaba. FEMS Microbiol. Ecol. 69 (3), 425–438. https://doi.org/10.1111/j.1574-6941.2009.00721.x.
Jorissen, F.J., de Stigter, H.C., Widmark, J.G.V., 1995. A conceptual model explaining benthic foraminiferal microhabitats. Mar. Micropaleontol. 26, 3–15. https://doi.org/10.1016/0377-8398(95)00047-X.
Jorissen, F., Nardelli, M.P., Almogi-Labin, A., Barras, C., Bergamin, L., Bicchi, E., El Kateb, A., Ferraro, L., McGann, M., Morigi, C., Romano, E., Sabbatini, A., Schweizer, M., Spezzaferri, S., 2018. Developing Foram-AMBI for biomonitoring in the Mediterranean: Species assignments to ecological categories. Mar. Micropaleontol. 140, 33–45. https://doi.org/10.1016/j.marmicro.2017.12.006.
Karner, M.B., Delong, E.F., Karl, D.M., 2001. Archaeal dominance in the mesopelagic zone of the Pacific Ocean. Nature 409 (6819), 507–510. https://doi.org/10.1038/35054051.
Kern, O.A., Koutsodendris, A., Mächtle, B., Christanis, K., Schukraft, G., Scholz, C., Kotthoff, U., Pross, J., 2019. XRF core scanning yields reliable semiquantitative data on the elemental composition of highly organic-rich sediments: Evidence from the Füramoos peat bog (Southern Germany). Sci. Total Environ. 697, 134110. https://doi.org/10.1016/j.scitotenv.2019.134110.
Kim, J.H., Schouten, S., Hopmans, E.C., Donner, B., Sinninghe Damsté, J.S., 2008. Global sediment core-top calibration of the TEX86 paleothermometer in the ocean. Geochim. Cosmochim. Acta 72, 1154–1173. https://doi.org/10.1016/j.gca.2007.12.010.
Kim, J.H., van der Meer, J., Schouten, S., Helmke, P., Willmott, V., Sangiorgi, F., Koç, N., Hopmans, E.C., Damsté, J.S.S., 2010. New indices and calibrations derived from the distribution of crenarchaeal isoprenoid tetraether lipids: Implications for past sea surface temperature reconstructions. Geochim. Cosmochim. Acta 74, 4639–4654. https://doi.org/10.1016/j.gca.2010.05.027.
Kim, J.G., Jung, M.Y., Park, S.J., Rijpstra, W.I.C., Sinninghe Damsté, J.S., Madsen, E.L., Min, D., Kim, J.S., Kim, G.J., Rhee, S.K., 2012. Cultivation of a highly enriched ammonia-oxidizing archaeon of thaumarchaeotal group I.1b from an agricultural soil. Environ. Microbiol. 14, 1528–1543. https://doi.org/10.1111/j.1462-2920.2012.02740.x.
Kim, J.H., Schouten, S., Rodrigo-Gámiz, M., Rampen, S., Marino, G., Huguet, C., Helmke, P., Buscail, R., Hopmans, E.C., Pross, J., Sangiorgi, F., Middelburg, J.B.M., Sinninghe Damsté, J.S., 2015. Influence of deep-water derived isoprenoid tetraether lipids on the TEX86H paleothermometer in the Mediterranean Sea. Geochim. Cosmochim. Acta 150, 125–141. https://doi.org/10.1016/j.gca.2014.11.017.
Kirkels, F.M.S.A., Usman, M.O., Peterse, F., 2022a. Distinct sources of bacterial branched GMGTs in the Godavari River basin (India) and Bay of Bengal sediments. Org. Geochem. 167, 104405. https://doi.org/10.1016/j.orggeochem.2022.104405.
Kirkels, F.M.S.A., Zwart, H.M., Usman, M.O., Hou, S., Ponton, C., Giosan, L., Eglinton, T. I., Peterse, F., 2022b. From soil to sea: sources and transport of organic carbon traced by tetraether lipids in the monsoonal Godavari River, India. Biogeosciences 19, 3979–4010. https://doi.org/10.5194/bg-19-3979-2022.
Klein, S.G., Frühe, L., Parry, A.J., Marchese, F., Nolan, M.K.B., Laiolo, E., Lim, K.K., Steckbauer, A., Breavington, J., Hempel, C.A., von Krusenstiern, K., van der Zwan, F. M., Re, E., Alamoudi, T., Alva Garcia, J.V., Arossa, S., Angulo-Preckler, C., Rodrigue, M., Pieribone, V.A., Qurban, M.A., Benzoni, F., Duarte, C.M., 2025. Deep oxygen-depleted depressions in a Red Sea coral reef sustain resistant ecosystems. PNAS Nexus 4 (3). https://doi.org/10.1093/pnasnexus/pgaf049.
Koga, Y., Nishihara, M., Morii, H., Akagawa-Matsushita, M., 1993. Ether polar lipids of methanogenic bacteria: Structures, comparative aspects, and biosyntheses.
Lambeck, K., Purcell, A., Flemming Nicholas, C., Vita-Finzi, C., Alsharekh, A.M., Bailey, G.N., 2011. Sea level and shoreline reconstructions for the Red Sea: Isostatic and tectonic considerations and implications for hominin migration out of Africa. Quat. Sci. Rev. 30, 3542–3574. https://doi.org/10.1016/j.quascirev.2011.08.008.
Laskar, J., Robutel, P., Joutel, F., Gastineau, M., Correia, A.C.M., Levrard, B., 2004. A long-term numerical solution for the insolation quantities of the Earth. Astron. Astrophys. 428, 261–285. https://doi.org/10.1051/0004-6361:20041335.
Legge, H.L., Mutterlose, J., Arz, H.W., 2006. Climatic changes in the northern Red Sea during the last 22,000 years as recorded by calcareous nannofossils. Paleoceanography 21, PA1003. https://doi.org/10.1029/2005PA001142.
Lei, Y., Yang, H., Dang, X., Zhao, S., Xie, S., 2016. Absence of a significant bias towards summer temperature in branched tetraether-based paleothermometer at two soil sites with contrasting temperature seasonality. Org. Geochem. 94, 83–94. https://doi.org/10.1016/j.orggeochem.2016.02.003.
Li, J., Pancost, R.D., Naafs, B.D.A., Yang, H., Zhao, C., Xie, S., 2016. Distribution of glycerol dialkyl glycerol tetraether (GDGT) lipids in a hypersaline lake system. Org. Geochem. 99, 113–124. https://doi.org/10.1016/j.orggeochem.2016.06.007.
Liu, X.L., Summons, R.E., Hinrichs, K.U., 2012. Extending the known range of glycerol ether lipids in the environment: Structural assignments based on tandem mass spectral fragmentation patterns. Rapid Commun. Mass Spectrom. 26, 2295–2302. https://doi.org/10.1002/rcm.6355.
Liu, X.L., Birgel, D., Elling, F.J., Sutton, P.A., Lipp, J.S., Zhu, R., Zhang, C., Könneke, M., Peckmann, J., Rowland, S.J., Summons, R.E., Hinrichs, K.U., 2016. From ether to acid: A plausible degradation pathway of glycerol dialkyl glycerol tetraethers. Geochim. Cosmochim. Acta 183, 138–152. https://doi.org/10.1016/j.gca.2016.04.016.
Lü, X., Liu, X.L., Elling, F.J., Yang, H., Xie, S., Song, J., Li, X., Yuan, H., Li, N., Hinrichs, K. U., 2015. Hydroxylated isoprenoid GDGTs in Chinese coastal seas and their potential as a paleotemperature proxy for mid-to-low latitude marginal seas. Org. Geochem. 89–90, 31–43. https://doi.org/10.1016/j.orggeochem.2015.10.004.
Margalef, R., 1978. Life-forms of phytoplankton as survival alternatives in an unstable environment. Oceanol. Acta 1, 385–391. https://doi.org/10.1007/BF00202661.
Mayer, D.E.B.Y., Beyin, A., 2009. Late stone age shell middens on the Red Sea Coast of Eritrea. J. Island Coast. Archaeol. 4, 108–124. https://doi.org/10.1080/15564890802662171.
Morcos, S.A., 1970. Physical and chemical oceanography of the Red Sea. Oceanogr. Mar. Biol. Annu. Rev. 8, 73–202.
Naafs, B.D.A., Inglis, G.N., Zheng, Y., Amesbury, M.J., Biester, H., Bindler, R., Blewett, J., Burrows, M.A., del Castillo Torres, D., Chambers, F.M., Cohen, A.D., Evershed, R.P., Feakins, S.J., Gałka, M., Gallego-Sala, A., Gandois, L., Gray, D.M., Hatcher, P.G., Honorio Coronado, E.N., Hughes, P.D.M., Huguet, A., Könönen, M., Laggoun-Défarge, F., Lähteenoja, O., Lamentowicz, M., Marchant, R., McClymont, E., Pontevedra-Pombal, X., Ponton, C., Pourmand, A., Rizzuti, A.M., Rochefort, L., Schellekens, J., De Vleeschouwer, F., Pancost, R.D., 2017. Introducing global peat-specific temperature and pH calibrations based on brGDGT bacterial lipids. Geochim. Cosmochim. Acta 208, 285–301. https://doi.org/10.1016/j.gca.2017.01.038.
Naafs, B.D.A., McCormick, D., Inglis, G.N., Pancost, R.D., 2018. Archaeal and bacterial H-GDGTs are abundant in peat and their relative abundance is positively correlated with temperature. Geochim. Cosmochim. Acta 227, 156–170. https://doi.org/10.1016/j.gca.2018.02.025.
Pan, F., Yuan, H., Song, J., Li, X., Duan, L., Wang, Y., 2025. BrGDGTs sources in eastern China marginal seas and their constraints on seawater temperature reconstruction. Chem. Geol. 676, 122624. https://doi.org/10.1016/j.chemgeo.2025.122624.
Paraschos, F., Koutsodendris, A., Sergiou, S., Geraga, M., Kaberi, H., Berke, M., Friedrich, O., Iliakis, S., Uy, M.A., Williams, R., Bailey, G., Sakellariou, D., 2025. Coupled sea-level and hydroclimatic controls on the southern Red Sea sedimentation during the past 30 ka. Quat. Sci. Rev. 357, 109310. https://doi.org/10.1016/j.quascirev.2025.109310.
Pearman, J.K., Ellis, J., Irigoien, X., Sarma, Y.V.B., Jones, B.H., Carvalho, S., 2017. Microbial planktonic communities in the Red Sea: high levels of spatial and temporal variability shaped by nutrient availability and turbulence. Sci. Rep. 7 (1), 6611. https://doi.org/10.1038/s41598-017-06928-z.
Peterse, F., Kim, J.H., Schouten, S., Kristensen, D.K., Koç, N., Sinninghe Damsté, J.S., 2009. Constraints on the application of the MBT/CBT palaeothermometer at high latitude environments (Svalbard, Norway). Org. Geochem. 40, 692–699. https://doi.org/10.1016/j.orggeochem.2009.03.004.
Pitcher, A., Hopmans, E.C., Mosier, A.C., Park, S.J., Rhee, S.K., Francis, C.A., Schouten, S., Sinninghe Damsté, J.S., 2011. Core and intact polar glycerol dibiphytanyl glycerol tetraether lipids of ammonia-oxidizing Archaea enriched from marine and estuarine sediments. Appl. Environ. Microbiol. 77 (10), 3468–3477. https://doi.org/10.1128/AEM.02758-10.
Qian, P.Y., Wang, Y., Lee, O.O., Lau, S.C.K., Yang, J., Lafi, F.F., Al-Suwailem, A., Wong, T.Y.H., 2011. Vertical stratification of microbial communities in the Red Sea revealed by 16S rDNA pyrosequencing. ISME J. https://doi.org/10.1038/ismej.2010.112.

R Core Team, 2022. R Core Team (2022) R: A Language and Environment for Statistical Computing. R Foundation for Statistical Computing, Vienna. https://www.R-project.org/.

Raitsos, D.E., Pradhan, Y., Brewin, R.J.W., Stenchikov, G., Hoteit, I., 2013. Remote sensing the phytoplankton seasonal succession of the red sea. PLoS One 8 (6), e64909. https://doi.org/10.1371/journal.pone.0064909.

Rohling, E.J., Grant, K., Hemleben, C., Kucera, M., Roberts, A.P., Schmeltzer, I., Schulz, H., Siccha, M., Siddall, M., Trommer, G., 2008. New constraints on the timing of sea level fluctuations during early to middle marine isotope stage 3. Paleoceanography 23, PA3219. https://doi.org/10.1029/2008PA001617.

Rohling, E.J., Grant, K.M., Roberts, A.P., Larrasoaña, J.-C., Larrasoañ, J.-C., 2013. Paleoclimate Variability in the Mediterranean and Red Sea Regions during the Last 500,000 Years. Curr. Anthropol. 54, S183–S201. https://doi.org/10.1086/673882.

Sakellariou, D., Rousakis, G., Panagiotopoulos, I., Morfis, I., Bailey, G., 2019. Geological Structure and Late Quaternary Geomorphological Evolution of the Farasan Islands Continental Shelf. South Red Sea, SW Saudi Arabia, in: Geological Setting, Palaeoenvironment and Archaeology of the Red Sea. 629–652.

Schattenhofer, M., Fuchs, B.M., Amann, R., Zubkov, M.V., Tarran, G.A., Pernthaler, J., 2009. Latitudinal distribution of prokaryotic picoplankton populations in the Atlantic Ocean. Environ. Microbiol. https://doi.org/10.1111/j.1462-2920.2009.01929.x.

Schouten, S., Hopmans, E.C., Schefuß, E., Sinninghe Damsté, J.S., 2002. Distributional variations in marine crenarchaeotal membrane lipids: a new tool for reconstructing ancient sea water temperatures? Earth Planet. Sci. Lett. 211, 205–206. https://doi.org/10.1016/s0012-821x(03)00193-6.

Schouten, S., Baas, M., Hopmans, E.C., Reysenbach, A.-L., Sinninghe-Damste, J.S., 2008. Tetraether membrane lipids of Candidatus " Aciduliprofundum boonei", a cultivated obligate thermoacidophilic euryarchaeote from deep-sea hydrothermal vents. Extremophiles 12, 119–124.

Schouten, S., Hopmans, E.C., Sinninghe Damsté, J.S., 2013. The organic geochemistry of glycerol dialkyl glycerol tetraether lipids: A review. Org. Geochem. 54, 19–61. https://doi.org/10.1016/j.orggeochem.2012.09.006.

Sergiou, S., Geraga, M., Rohling, E.J., Rodríguez-Sanz, L., Hadjisolomou, E., Paraschos, F., Sakellariou, D., Bailey, G., 2022a. Influences of sea level changes and the South Asian Monsoon on southern Red Sea oceanography over the last 30 ka. Quaternary Research (United States) 1–19. https://doi.org/10.1017/qua.2022.16.

Sergiou, S., Geraga, M., Rohling, E.J., Rodríguez-Sanz, L., Prandekou, A., Noti, A., Paraschos, F., Sakellariou, D., Bailey, G.N., 2022b. Marine Micropaleontology The evolution of seafloor environmental conditions in the southern Red Sea continental shelf during the last 30 ka. Mar. Micropaleontol. 177, 102181. https://doi.org/10.1016/j.marmicro.2022.102181.

Siddall, M., Rohling, E.J., Almogi-Labin, A., Hemleben, C., Meischner, D., Schmelzer, I., Smeed, D.A., 2003. Sea-level fluctuations during the last glacial cycle. Nature 423, 853–858. https://doi.org/10.1038/nature01690.

Siddall, M., Smeed, D.A., Hemleben, C., Rohling, E.J., Schmelzer, I., Peltier, W.R., 2004. Understanding the Red Sea response to sea level. Earth Planet. Sci. Lett. 225, 421–434. https://doi.org/10.1016/j.epsl.2004.06.008.

Singh, A.D., Rai, A.K., Verma, K., Das, S., Bharti, S.K., 2015. Benthic foraminiferal diversity response to the climate induced changes in the eastern Arabian Sea oxygen minimum zone during the last 30 ka BP. Quat. Int. 374, 118–125. https://doi.org/10.1016/j.quaint.2014.11.052.

Sinninghe Damsté, J.S., 2016. Spatial heterogeneity of sources of branched tetraethers in shelf systems: The geochemistry of tetraethers in the Berau River delta (Kalimantan, Indonesia). Geochim. Cosmochim. Acta 186, 13–31. https://doi.org/10.1016/j.gca.2016.04.033.

Sinninghe Damsté, J.S., Schouten, S., Hopmans, E.C., Van Duin, A.C.T., Geenevasen, J.A.J., 2002. Crenarchaeol: The characteristic core glycerol dibiphytanyl glycerol tetraether membrane lipid of cosmopolitan pelagic crenarchaeota. J. Lipid Res. 43, 1641–1651. https://doi.org/10.1194/jlr.M200148-JLR200.

Sinninghe Damsté, J.S., Ossebaar, J., Schouten, S., Verschuren, D., 2012a. Distribution of tetraether lipids in the 25-ka sedimentary record of Lake Challa: Extracting reliable TEX 86 and MBT/CBT palaeotemperatures from an equatorial African lake. Quat. Sci. Rev. 50, 43–54. https://doi.org/10.1016/j.quascirev.2012.07.001.

Sinninghe Damsté, J.S., Rijpstra, W.I.C., Hopmans, E.C., Jung, M.Y., Kim, J.G., Rhee, S. K., Stieglmeier, M., Schleper, C., 2012b. Intact polar and core glycerol dibiphytanyl glycerol tetraether lipids of group I.1a and I.1b Thaumarchaeota in soil. Appl. Environ. Microbiol. 78, 6866–6874. https://doi.org/10.1128/AEM.01681-12.

Sofianos, S.S., Johns, W.E., 2007. Observations of the summer Red Sea circulation. J. Geophys. Res. 112, C06025. https://doi.org/10.1029/2006JC003886.

Southon, J., Kashgarian, M., Fontugne, M., Metivier, B., Yim, Wyss W.-S., 2002. Marine reservoir corrections for the Indian Ocean and southeast Asia. Radiocarbon 44, 167–180.

Taylor, K.W.R., Huber, M., Hollis, C.J., Hernandez-Sanchez, M.T., Pancost, R.D., 2013. Re-evaluating modern and Palaeogene GDGT distributions: Implications for SST reconstructions. Glob. Planet. Chang. 108, 158–174. https://doi.org/10.1016/j.gloplacha.2013.06.011.

Teske, A., Sørensen, K.B., 2008. Uncultured archaea in deep marine subsurface sediments: Have we caught them all? ISME J. 2, 3–18. https://doi.org/10.1038/ismej.2007.90.

Tierney, J.E., DeMenocal, P.B., 2013. Abrupt shifts in Horn of Africa hydroclimate since the last glacial maximum. Science 342, 843–846. https://doi.org/10.1126/science.1240411.

Tierney, J.E., Russell, J.M., Eggermont, H., Hopmans, E.C., Verschuren, D., Sinninghe Damsté, J.S., 2010. Environmental controls on branched tetraether lipid distributions in tropical East African lake sediments. Geochim. Cosmochim. Acta 74, 4902–4918. https://doi.org/10.1016/j.gca.2010.06.002.

Trommer, G., Siccha, M., van der Meer, M.T.J., Schouten, S., Sinninghe Damsté, J.S., Schulz, H., Hemleben, C., Kucera, M., 2009. Distribution of Crenarchaeota tetraether membrane lipids in surface sediments from the Red Sea. Org. Geochem. 40, 724–731. https://doi.org/10.1016/j.orggeochem.2009.03.001.

Trommer, G., Siccha, M., Rohling, E.J., Grant, K., Van Meer, M.T.J., Der, Schouten, S., Hemleben, C., Kucera, M., Schouten, S., van der Meer, M.T.J., Hemleben, C., Grant, K., Rohling, E.J., Siccha, M., Trommer, G., 2010. Millennial - scale variability in Red Sea circulation in response to Holocene insolation forcing. Paleoceanography 25, 1–17. https://doi.org/10.1029/2009PA001826.

Trommer, G., Siccha, M., Rohling, E.J., Grant, K., Van Der Meer, M.T.J., Schouten, S., Baranowski, U., Kucera, M., 2011. Sensitivity of Red Sea circulation to sea level and insolation forcing during the last interglacial. Clim. Past 7, 941–955. https://doi.org/10.5194/cp-7-941-2011.

Turich, C., Freeman, K.H., 2011. Archaeal lipids record paleosalinity in hypersaline systems. Org. Geochem. 42, 1147–1157. https://doi.org/10.1016/j.orggeochem.2011.06.002.

Van Bree, L.G.J., Peterse, F., Baxter, A.J., De Crop, W., Van Grinsven, S., Villanueva, L., Verschuren, D., Sinninghe Damsté, J.S., 2020. Seasonal variability and sources of in situ brGDGT production in a permanently stratified African crater lake. Biogeosciences 17, 5443–5463. https://doi.org/10.5194/bg-17-5443-2020.

Varma, D., Hopmans, E.C., van Kemenade, Z.R., Kusch, S., Berg, S., Bale, N.J., Sangiorgi, F., Reichart, G.J., Sinninghe Damsté, J.S., Schouten, S., 2024a. Evaluating isoprenoidal hydroxylated GDGT-based temperature proxies in surface sediments from the global ocean. Geochim. Cosmochim. Acta 370, 113–127. https://doi.org/10.1016/j.gca.2023.12.019.

Varma, D., van der Meer, M.T.J., Reichart, G.J., Schouten, S., 2024b. Impact of water depth on the distributions and proxies of isoprenoidal hydroxylated GDGTs in the Mediterranean Sea and the Red Sea. Org. Geochem. 194, 104780. https://doi.org/10.1016/j.orggeochem.2024.104780.

Verma, K., Singh, H., Singh, A.D., Singh, P., Satpathy, R.K., Naidu, P.D., 2021. Benthic Foraminiferal Response to the Millennial-Scale Variations in Monsoon-Driven Productivity and Deep-Water Oxygenation in the Western Bay of Bengal During the Last 45 ka. Front. Mar. Sci. 8, 19–22. https://doi.org/10.3389/fmars.2021.733365.

Vermeersch, P.M., Van Peer, P., Rots, V., Van Kerckhoven, L., Van Neer, W., 2005. The Middle Holocene shell mound of El Gouna on the Red Sea (Egypt). J. Field Archaeol. 30, 435–442. https://doi.org/10.1179/009346905791072143.

Walker, M.J.C., Berkelhammer, M., Björck, S., Cwynar, L.C., Fisher, D.A., Long, A.J., Lowe, J.J., Newnham, R.M., Rasmussen, S.O., Weiss, H., 2012. Formal subdivision of the Holocene Series/Epoch: A Discussion Paper by a Working Group of INTIMATE (Integration of ice-core, marine and terrestrial records) and the Subcommission on Quaternary Stratigraphy (International Commission on Stratigraphy). J. Quat. Sci. 27, 649–659. https://doi.org/10.1002/jqs.2565.

Wang, H., Liu, W., Lu, H., 2016. Appraisal of branched glycerol dialkyl glycerol tetraether-based indices for North China. Org. Geochem. 98, 118–130. https://doi.org/10.1016/j.orggeochem.2016.05.013.

Weber, Y., Damsté, J.S.S., Zopfi, J., De Jonge, C., Gilli, A., Schubert, C.J., Lepori, F., Lehmann, M.F., Niemann, H., 2018. Redox-dependent niche differentiation provides evidence for multiple bacterial sources of glycerol tetraether lipids in lakes. Proc. Natl. Acad. Sci. USA 115, 10926–10931. https://doi.org/10.1073/pnas.1805186115.

Weijers, Johan W.H., Schouten, S., Hopmans, E.C., Geenevasen, J.A.J., David, O.R.P., Coleman, J.M., Pancost, R.D., Sinninghe Damsté, J.S., 2006a. Membrane lipids of mesophilic anaerobic bacteria thriving in peats have typical archaeal traits. Environ. Microbiol. 8, 648–657. https://doi.org/10.1111/j.1462-2920.2005.00941.x.

Weijers, Johan W.H., Schouten, S., Spaargaren, O.C., Sinninghe Damsté, J.S., 2006b. Occurrence and distribution of tetraether membrane lipids in soils: Implications for the use of the TEX86 proxy and the BIT index. Org. Geochem. 37, 1680–1693. https://doi.org/10.1016/j.orggeochem.2006.07.018.

Weijers, J.W.H., Schouten, S., van den Donker, J.C., Hopmans, E.C., Sinninghe Damsté, J. S., 2007. Environmental controls on bacterial tetraether membrane lipid distribution in soils. Geochim. Cosmochim. Acta 71, 703–713. https://doi.org/10.1016/j.gca.2006.10.003.

Weijers, J.W.H., Schefuß, E., Kim, J.H., Sinninghe Damsté, J.S., Schouten, S., 2014. Constraints on the sources of branched tetraether membrane lipids in distal marine sediments. Org. Geochem. 72, 14–22. https://doi.org/10.1016/j.orggeochem.2014.04.011.

Weisse, T., 1989. The microbial loop in the Red Sea. dynamics of pelagic bacteria and heterotrophic nanoflagellates. Mar. Ecol. Prog. Ser. 55, 241–250. https://doi.org/10.3354/meps055241.

Werner, F., Lange, K., 1975. A bathymetry survey of the sill area between the Red Sea and Gulf of Aden. Geol. Jahrb. D 25–30.

Wu, J., Yang, H., Pancost, R.D., Naafs, B.D.A., Qian, S., Dang, X., Sun, H., Pei, H., Wang, R., Zhao, S., Xie, S., 2021. Variations in dissolved O2 in a Chinese lake drive changes in microbial communities and impact sedimentary GDGT distributions. Chem. Geol. 579, 120348. https://doi.org/10.1016/j.chemgeo.2021.120348.

Xiao, W., Xu, Y., Ding, S., Wang, Y., Zhang, X., Yang, H., Wang, G., Hou, J., 2015. Global calibration of a novel, branched GDGT-based soil pH proxy. Org. Geochem. 89–90, 56–60. https://doi.org/10.1016/j.orggeochem.2015.10.005.

Xiao, W., Wang, Y., Zhou, S., Hu, L., Yang, H., Xu, Y., 2016. Ubiquitous production of branched glycerol dialkyl glycerol tetraethers (brGDGTs) in global marine environments: A new source indicator for brGDGTs. Biogeosciences 13, 5883–5894. https://doi.org/10.5194/bg-13-5883-2016.

Yang, H., Lü, X., Ding, W., Lei, Y., Dang, X., Xie, S., 2015. The 6-methyl branched tetraethers significantly affect the performance of the methylation index (MBT') in soils from an altitudinal transect at Mount Shennongjia. Org. Geochem. 82, 42–53. https://doi.org/10.1016/j.orggeochem.2015.02.003.

Yao, F., Hoteit, I., Pratt, L.J., Bower, A.S., Kohl, A., Gopalakrishnan, G., Rivas, D., 2014. Seasonal overturning circulation in the Red Sea: 2. Winter circulation. J. Geophys. Res. Oceans 119 (4), 2263–2289. https://doi.org/10.1002/2013jc009331.

Yao, Y., Zhao, J., Vachula, R.S., Werne, J.P., Wu, J., Song, X., Huang, Y., 2020. Correlation between the ratio of 5-methyl hexamethylated to pentamethylated branched GDGTs (HP5) and water depth reflects redox variations in stratified lakes. Org. Geochem. 147, 104076. https://doi.org/10.1016/j.orggeochem.2020.104076.

Zhang, Y.G., Zhang, C.L., Liu, X.L., Li, L., Hinrichs, K.U., Noakes, J.E., 2011. Methane Index: A tetraether archaeal lipid biomarker indicator for detecting the instability of marine gas hydrates. Earth Planet. Sci. Lett. 307, 525–534. https://doi.org/10.1016/j.epsl.2011.05.031.

Zhang, Z., Smittenberg, R.H., Bradley, R.S., 2016. GDGT distribution in a stratified lake and implications for the application of TEX 86 in paleoenvironmental reconstructions. Sci. Rep. 6, 34465. https://doi.org/10.1038/srep34465.

Zhu, C., Weijers, J.W.H., Wagner, T., Pan, J.M., Chen, J.F., Pancost, R.D., 2011. Sources and distributions of tetraether lipids in surface sediments across a large river-dominated continental margin. Org. Geochem. 42, 376–386. https://doi.org/10.1016/j.orggeochem.2011.02.002.

Ziegler, M., Jilbert, T., De Lange, G.J., Lourens, L.J., Reichart, G.J., 2008. Bromine counts from XRF scanning as an estimate of the marine organic carbon content of sediment cores. Geochem. Geophys. Geosyst. 9, 1–6. https://doi.org/10.1029/2007GC001932.